BaBar Analysis Document #2651, Version 13 March 28, 2017

# Study of $e^+e^- \to \pi^+\pi^-\eta$ process using initial state radiation with BaBar

E. A. Kozyrev, E. P. Solodov[a][b]
Budker Institute of Nuclear Physics SB RAS, Novosibirsk 630090[a],Novosibirsk State University, Novosibirsk 630090[b], Russia

March 28, 2017

---

## Abstract

We study the process $e^+e^- \to \pi^+\pi^-\eta\gamma$, where the photon is radiated from the initial state, providing cross section measurements for the hadronic states over a continuum of center-of-mass energies. About 10k fully reconstructed events are selected from 469 $\mathrm{fb}^{-1}$ of *BABAR* data. Using $\pi^+\pi^-\eta$ mass spectrum we evaluated the $e^+e^- \to \pi^+\pi^-\eta$ cross section in the energy range from 1.15 to 3.5 GeV. The cross section is well described by the vector meson dominance model with three excited $\rho$-like states, and is used to test the CVC hypothesis. We observe $49 \pm 9$ events of $J/\psi$ decay to $\pi^+\pi^-\eta$, and measure a product $\Gamma_{J/\Psi\to e^+e^-} B_{J/\Psi\to\pi^+\pi^-\eta} = 2.34 \pm 0.46$ eV.

---

## Contents

## 1. Introduction

The analysis of the process $e^+e^- \to \gamma$ + hadrons with emitted from initial state high energy photon gives the opportunity effectively reduce the electron-positron invariant mass and study hadron production over a wide

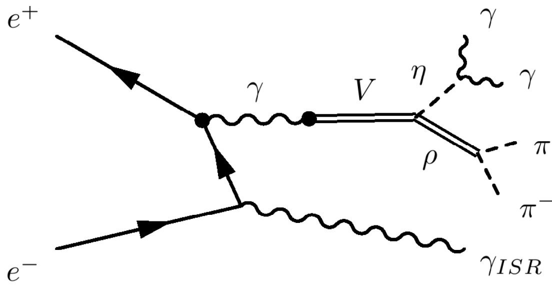

Figure 1: The Feynman diagram of the process $e^+e^- \to \eta\pi^-\pi^+(\gamma)$

range of center-of-mass (c.m.) energy in a single experiment. The possibility of using the initial state radiation of hard photons at B-factories has been discussed previously [1]. The photon emission is described by radiator function W(s, x, $\theta$), that is calculated in quantum electrodynamics with accuracy greater 0.5 % and is defined as following:

$$\frac{d\sigma_{e^+e^-\to\eta\pi^-\pi^+(\gamma)}(x)}{dx} = W(s,x)\sigma_{e^+e^-\to\eta\pi^-\pi^+}(\sqrt{s(1-x)}), \tag{1}$$

where $x = \frac{2E_\gamma}{\sqrt{s}}$, $\sqrt{s} = 10.58$ GeV and $E_\gamma-$ energy of ISR photon in c.m. frame. The function W(s, x, $\theta$) falls rapidly as $E_\gamma$ increases from zero, but has a long tail which combines with the increasing $\sigma(\sqrt{s(1-x)})$, that allows to produce a sizable cross section at very low $E_{c.m.}$. The angular distribution of the ISR photon peaks along the beam directions, but ∼15% of the photons are within a typical detector acceptance.

This document is dedicated to the study of the process $e^+e^- \to \eta\pi^-\pi^+(\gamma)$ (Fig. 1) where photon is emitted from initial electron-positron state and $\eta$ decays into two photons ($\mathrm{Br}_{\eta\to2\gamma} = 39.31 \pm 0.20$ %). The process was already studied at BaBar [9]. The previous study was based on only the half of total integrated luminosity and on the channel $\eta \to \pi^+\pi^-\pi^0$ ($\mathrm{Br}_{\eta\to3\pi} = 22.74 \pm 0.28$ %).

The work is important for the study of vector mesons excitations, especially $\rho$-like excitations, for the test of the hypothesis of conserved vector current (CVC) in comparison with spectral functions of $\tau$ the decay into $\pi^-\pi^0\eta\nu_\tau$. And there are other physics motivations, among them: the calculation of the contribution into hadronic vacuum polarization and the test of Vector Meson Dominance model.

## 2. Data sets and MC samples

This analysis is based on the data including runs 1-6 with total integrated luminosity 468.1 $fb^{-1}$ collected with the BABAR detector at the SLAC National Accelerator Laboratory at the PEP-II asymmetric-energy $e^+e$ collider. About 90% of the data were collected at the $e^+e^-$ c.m. energy 10.58 GeV (the $\Upsilon(4S)$ mass), and 10% at 10.54 GeV. The BABAR detector is described in details elsewhere [14]. Charged-particle tracks are measured with a five-layer double-sided silicon vertex tracker (SVT) together with a 40-layer drift chamber (DCH), both inside a 1.5 T superconducting solenoid magnet. Photons are assumed to originate from the primary vertex defined by the charged tracks of the event and their energy and position are measured in a CsI(Tl) electromagnetic calorimeter (EMC). Charged-particle identification (PID) uses the ionization energy loss dE/dx in the SVT and DCH, the Cherenkov radiation detected in a ring-imaging device (DIRC), the shower energy deposit in the EMC, and the shower shape in the instrumented flux return (IFR) of the magnet that provides muon identification.

Both data and Monte-Carlo samples are processed under 24th release. The used simulated sample is listed in the Table 1. The third column corresponds to visible cross section of the process $e^+e \to X\gamma$ with ISR photon at large angle. It was calculated as:

$$\sigma_{e^+e^-\to X(\gamma)} = \int\int_{cos(20^\circ)}^{cos(160^\circ)} W(s,x)\sigma_{e^+e^-\to X}(\sqrt{s(1-x)})dcos(\theta_\gamma)dx \tag{2}$$

| process | $N_{gen}$ | $\sigma$, pb |
|---|---|---|
| $2\pi\eta\gamma$ | 855973 | $0.172\pm0.015_{stat}$ |
| $2\pi 2\pi^0\gamma$ | 4279929 | 4.2 ±0.5 |
| uds | 1282347 | 2090 |
| $3\pi\eta\gamma$ | 426993 | 0.2 ±0.02 |
| $3\pi\gamma$ | 899996 | 2.6 ±0.5 |
| $\omega 2\pi^0\gamma$ | 672357 | |
| 2K | 1332161 | |
| $2K\eta$ | 426992 | 0.08±0.01 |
| $2K\pi^0$ | 1310662 | |
| $2\pi$ | 1844824 | 21.4 |
| $2\tau$ | 10104949 | 890 |

Table 1: The information about used simulated sample

The ISR processes were generated with AfkQed event generator [15]. The structure function [16] method is used to calculate QED corrections for extra photon emission from the initial state. The one or two extra photons are generated along the directions of electron or positron. The final particles bremsstrahlung is generated using the PHOTOS package [17]. Simulated events are performed with the following photon polar angles in center-of-mass system: $20^\circ < \theta < 160^\circ$. Also The BaBaR ISR simulation in AfkQED is done with the requirement on the combined invariant mass of the hadronic system and the ISR photon to be greater 8 $GeV/c^2$. The requirement suppresses the production of events with high-energetic NLO radiation and initial state radiative correction is close to unity with accuracy about 1%. In addition, the samples of $e^+e^- \to q\bar{q}$ (q = u,d,s) events were generated via JETSET and $e^+e^- \to \tau^+\tau^-$ events via KORALB [20]. The ISR events was deleted from $q\bar{q}$ simulation due to impossibility to reproduce hadron spectrum at low energies. The simulation considers the variation of the detector and accelerator conditions.

### *2.1.* $2\pi^\pm 2\pi^0\gamma$ *background*

The visible radiative cross section of the background has been calculated using preliminary BaBar data [21, 22]. The calculation based on the formula (2) leads to result $\sigma_{2\pi^\pm 2\pi^0\gamma} = 4.2 \pm 0.5$ pb.

### *2.2.* $2\pi^\pm\pi^0\eta\gamma$ *background*

The process proceeds via three main intermediate states $\omega\eta\gamma$, $\phi\eta\gamma$ and $a\rho$. The visible cross section of the background has been calculated using preliminary SND data [24]. As a result we obtain 0.20 ±0.02 pb. The error includes only errors of born cross section. We use MC simulation only of $\omega\eta\gamma$ state, assuming that detection efficiency doesn't strongly depend on dynamics.

### *2.3.* $2K\eta\gamma$ *background*

The visible cross section of the background has been calculated using BaBar data (BAD 1613). As a result we obtain 0.08 ± 0.01 pb. The error includes only errors of born cross section.

## 3. Event selection

- The first selection criteria consists in the requirement of the presence of detected high energy photon with energy greater than 3 GeV in center of mass frame and at least two tracks and two additional photons with invariant mass in the range [0.44 : 0.64] GeV/$c^2$ near $\eta$ mass. Each of the both photons is required to have energy greater than 100 MeV and polar angle in the range 0.3-2.1 radians.

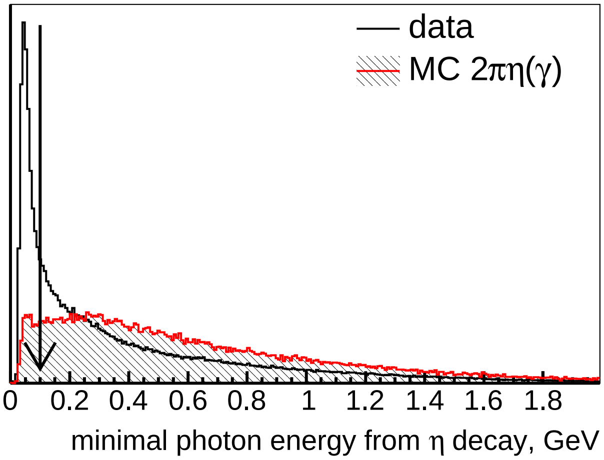

Figure 2: The comparison of simulated and experimental distributions of minimal photon energy from $\eta$ decay into two photons. The selection $E\gamma_{1,2} > 0.1$ GeV for each photon from $\eta$ decay is applied for event selection.

The comparison of simulated and experimental distributions of minimal photon energy from $\eta$ decay into two photons is shown in the Fig. 2. Soft photon background is mainly related with $e^+e^- \to 2\pi^\pm 2\pi^0\gamma_{ISR}$ process with low energy $\pi^0$ momentum. If several photons are detected, the ISR photon is assumed to be that with the highest energy. Most events contain additional soft photons due to machine background or/and interactions in the detector material or/and FSR or/and NLO ISR.

Geometrical efficiency of the registration of the $2\pi\eta(\to 2\gamma)\gamma_{ISR}$ system equals to $\epsilon_{reg}^{geom}(0.3 < \theta_\gamma < 2.3, 0.4 < \theta_\pi < 2.4) \cdot Br_{\eta\to 2\gamma} \approx 18\%$.

- Each charged track reconstructed in the DCH or SVT or both is required to extrapolate within ± 3 cm in z and 0.25 cm in radius of the nominal interaction point. The charged track vertex is used at the point of origin to calculate the angles for all detected photons. Additionally, the tracks are required to be not identified both simultaneously as kaons or muons. If there are three or more tracks, two of them with opposite charges and closest distance to the interaction region are used for the further analysis.

The initial sample of candidate events is subjected to a constrained kinematic fits. The first 4C fit includes 4 energy-momentum conservations:

$$P_{e^+} + P_{e^-} = P_{\pi^+} + P_{\pi^-} + P_{\gamma_{ISR}} + P_{\gamma_1} + P_{\gamma_2}$$

For the ISR photon we use asymmetric (Novosibirsk) function to describe EMC response and additional alignment [23]. Also covariance matrices of the initial $e^+, e^-$ and final state charged particles are taken into account. The combination of the particles with the smallest $\chi^2_{4C}$ is tagged and is used in the selection steps. The parameter $\chi^2_{4C}$ is used to discriminate between signal and background events.

- Because of very different background conditions, the $\pi^+\pi^-\eta$ invariant mass interval under study is divided into two regions: $1.15 < m_{\pi^+\pi^-\eta} < 2.0$ GeV/$c^2$ (I) and $2.0 < m_{\pi^+\pi^-\eta} < 3.5$ GeV/$c^2$ (II). The requirements $\chi^2_{4C} < 25$ for Region I and $\chi^2_{4C} < 15$ for Region II are used for the signal selection.

- We use several additional selections for Region II. The invariant mass of the tagged ISR photon and $\pi^\pm$ is shown in the Fig. 3. For Region II we require $m_{\pi^\pm\gamma_{isr}} > 1$ GeV/c$^2$.

- The energy spectrum of the first photon tagged from $\eta$ decay is shown in the Fig. 4. For Region II we require that the energy of each photon from $\eta$ decay $E_{\gamma_{1,2}} > 0.2$ GeV.

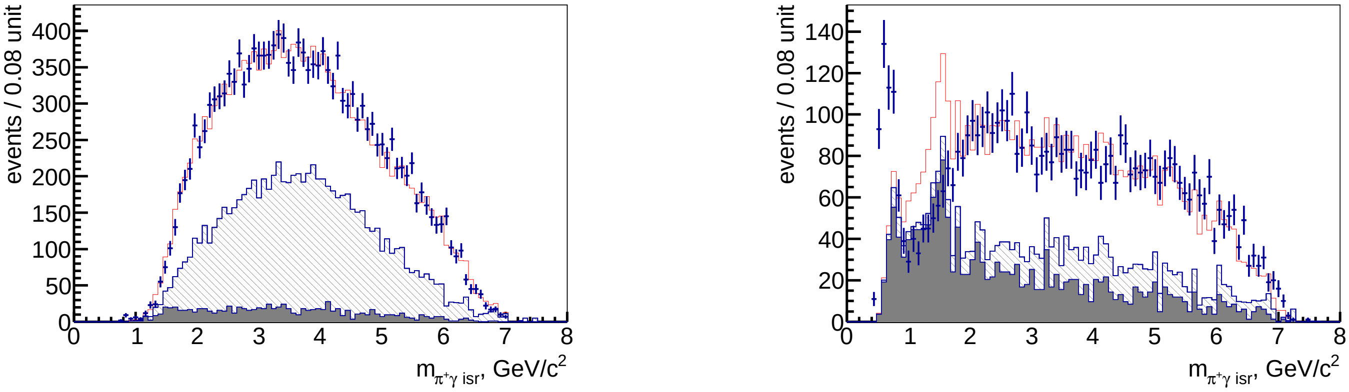

Figure 3: The invariant mass of the tagged ISR photon and $\pi^+$ for Region I (left) and Region II (right). The lightly shaded histogram is for ISR background and filled histogram represents non-ISR background.

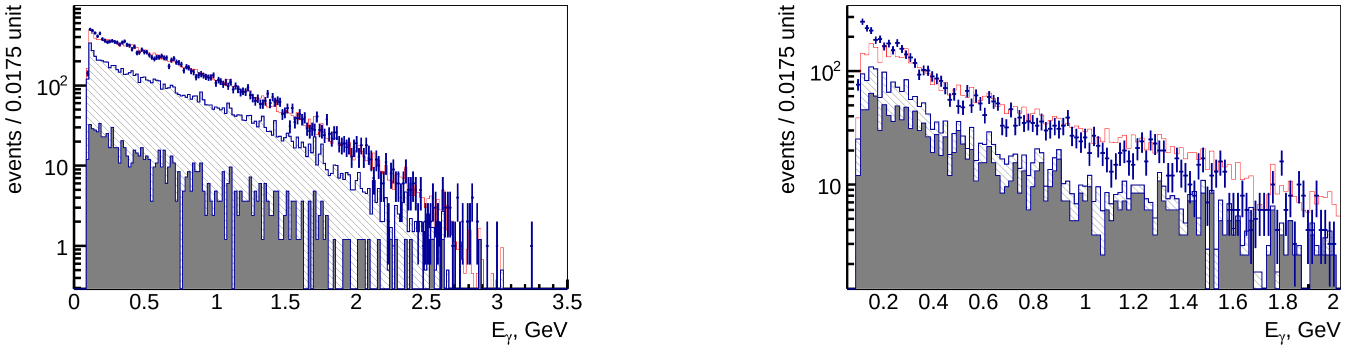

Figure 4: The energy spectrum of the first photon tagged from $\eta$ decay for Region I (left) and Region II (right). The lightly shaded histogram is for ISR background and filled histogram represents non-ISR background.

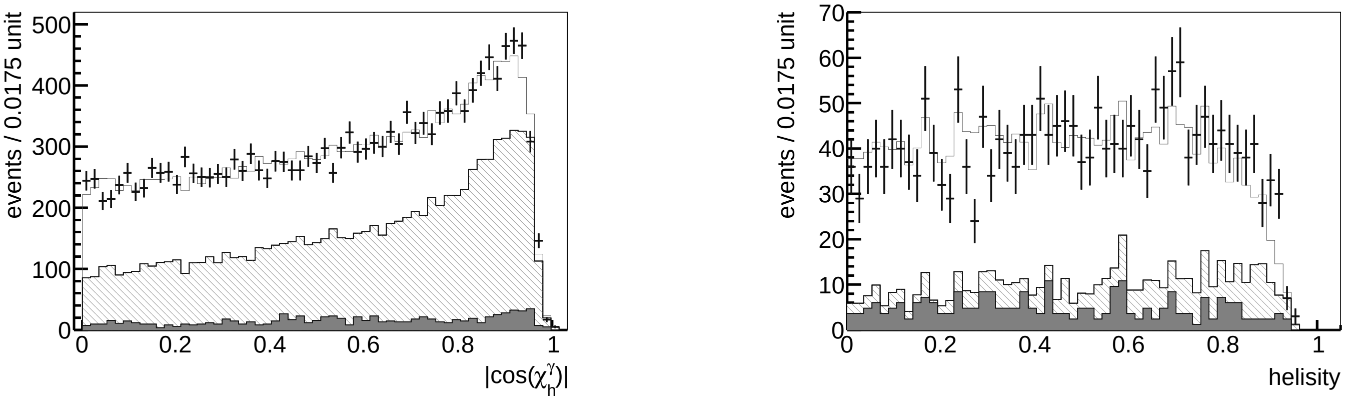

Figure 5: The absolute value of the cosine of the angle between the decay photon momentum in the $\eta$ rest frame and the $\eta$ direction in the lab frame for Region I (left) and Region II (right). The lightly shaded histogram is for ISR background and filled histogram represents non-ISR background.

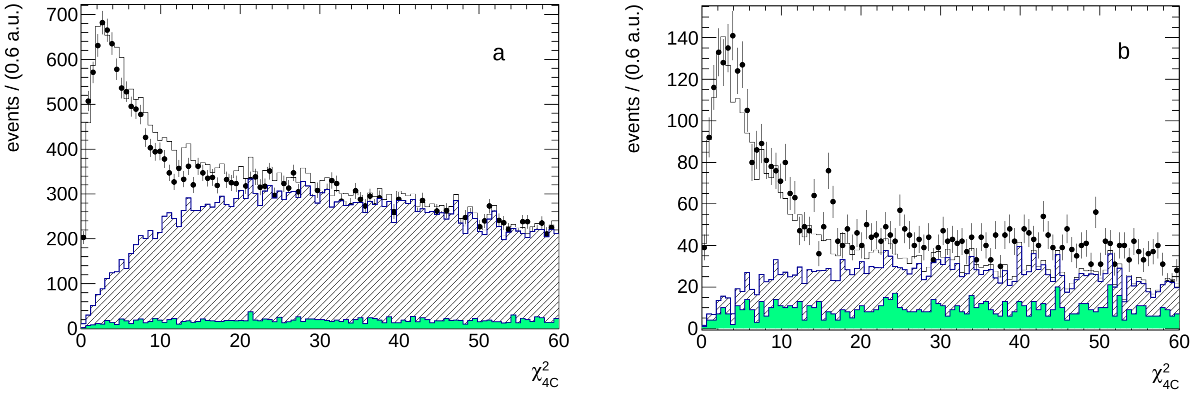

Figure 6: The $\chi^2_{4C}$ distributions for events from the invariant mass range $1.15 < m_{\pi^+\pi^-\eta} < 2.00$ GeV/$c^2$ (a) and $2.0 < m_{\pi^+\pi^-\eta} < 3.5$ GeV/$c^2$ (b). The points with error bars are data. The unshaded histogram represents the sum of the $\chi^2_{4C}$ distributions for simulated signal and backgrounds events. The filled histogram represents non-ISR background, the hatched histogram - ISR background.

- The absolute value of the cosine of the angle between the decay photon momentum in the $\eta$ rest frame and the $\eta$ direction in the lab frame is distributed in the Fig. 5. The distribution doesn't allow to apply effective additional selections.

- We require that the invariant mass of two selected pions $m_{2\pi}$ is greater than 0.4 GeV/c$^2$, the $m_{2\pi}$ distribution will be discussed below.

The $\chi^2_{4C}$ distributions for events from Region I (a) and Region II (b) are shown in Fig. 6. Points with error bars represent data, while the histograms show, cumulatively, the contributions of simulated non-ISR background (filled), ISR background (hatched), and signal $e^+e^- \to \pi^+\pi^-\eta\gamma$ events (open histogram). For background, the distributions are normalized to expected numbers of events calculated using known experimental cross sections (see the Table 1). For the $e^+e^- \to q\bar{q}$ background, the expected number is corrected to take into account data-MC simulation difference (see below). The signal distribution is normalized in such a way that the total simulated distribution matches the first seven bins of the data distribution. It is seen that background is underestimated at large $\chi^2_{4C}$. At low $\chi^2_{4C}$ values the simulation reproduces the data reasonably well.

The background level in the considered mass interval is still relatively high, and we use additional selection criteria. The dominant background is related with the process $e^+e^- \to \pi^+\pi^- 2\pi^0\gamma_{ISR}$. So, we need to create new variable wich is sensitive to possible presence of additional $\pi^0$ in an event. In order to create the variable ($m^{\pi^0}_{2\gamma}$) we find the pair of photons with the invariant mass closest to the $\pi^0$ mass. We run over all photons with energy larger 100 MeV. The $m^{\pi^0}_{2\gamma}$ is distributed in the Fig. 7.

- For both Regions I and II we require $m^{\pi^0}_{2\gamma} > 0.16$ GeV/c$^2$. For the following this selection will be referred to as "golden selection".

As a result, 11469 data events are selected.

Figure 8 shows the distributions of the $\eta$-meson candidate invariant mass ($m_{\gamma\gamma}$), which is calculated using photon parameters returned by the 4C kinematic fit. The points with error bars represent data. The open area show the $m_{\gamma\gamma}$ distribution for signal simulated events. The lightly shaded histogram is for ISR background and filled histogram represents non-ISR background.

### *3.1. $q\bar{q}$ normalization.*

The cross sections for the background processes in continuum production of $q\bar{q}$ are poorly known. All $q\bar{q}$ events passed our selection events should be divided into two types: 1) $e^+e^- \to \pi^-\pi^+\pi^0\eta$ - the events is

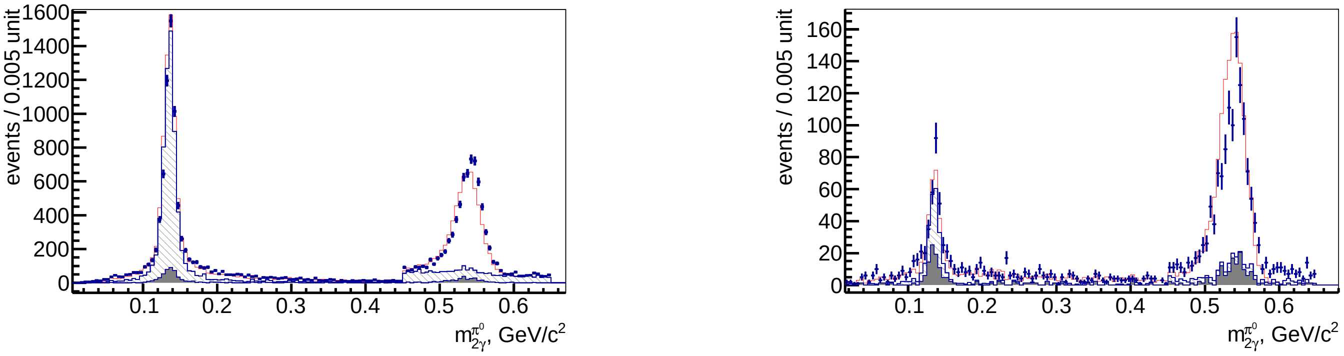

Figure 7: The two-photon invariant mass closest to the $\pi^0$ mass for Region I (left) and Region II (right). The lightly shaded histogram is for ISR background and filled histogram represents non-ISR background.

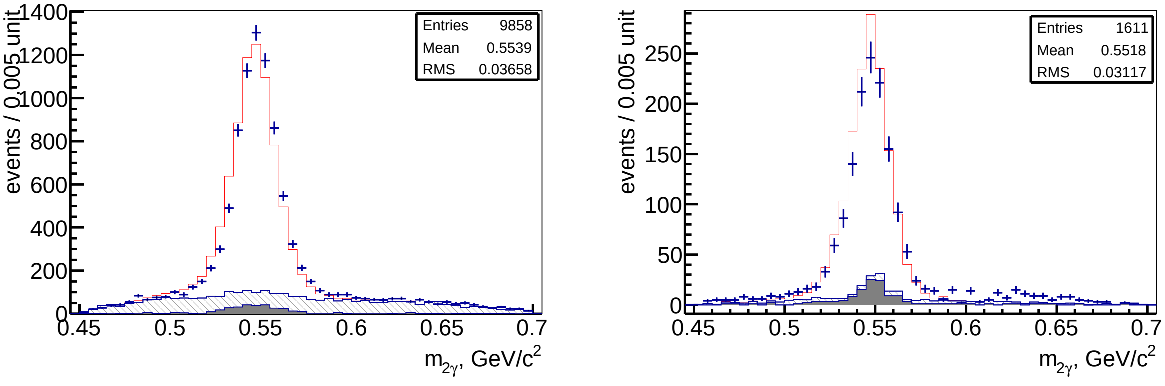

Figure 8: The two photon invariant mass distribution after 4C fit for events from Region I (left), and Region II (right) after all requirements. The points with error bars are data, when the histograms comulatively show contributions from ISR background (light shaded), non-ISR background (dark shaded), and simulated signal $e^+e^- \to \pi^+\pi^-\eta\gamma$ events.

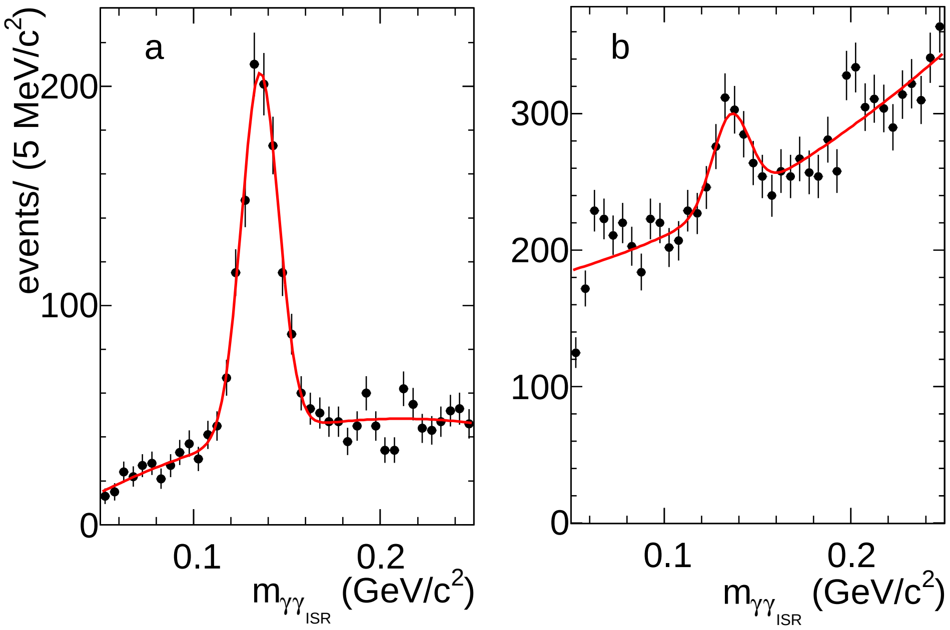

Figure 9: The invariant mass of the ISR photon and any other photon in the event for $q\bar{q}$ simulation (left) and data (right).

characterized by peaked at $m_{\pi^0}$ two photon invariant mass distribution after 4C; 2) $e^+e^- \to \pi^+\pi^-n\pi^0$, $\rho^+\rho^-\pi^0$, $\rho^+\rho^-\pi^0\pi^0$, $K^+K^-n\pi^0$ and etc. - the events is characterized by flat (non-peaking) invariant mass distribution of two photons tagged by 4C fit. These classes of $q\bar{q}$ events, as a result, produces a sharp peak at the $\pi^0$ invariant mass when the fake ISR photon is combined with another photon in the event.

Figure 9 shows the invariant mass distribution, obtained from a combination of the ISR photon candidate with any other photon for data (right) and $q\bar{q}$ simulation (left): to increase statistics we use events with $\chi^2_{4C} < 100$ and without "golden selection". The $\pi^0$ peaks are clearly seen in both distributions, indicating the presence of non-ISR processes. We approximate the distribution of Fig. 9(right) with the sum of simulated distribution of Fig. 9(left) and second-order polynomial function. The figure 10 also demonstrates the normalisation factor as a function of $m_{2\pi\eta}$ range. The dependence allows to assume, that the normalization doesn't depend on $m_{2\pi\eta}$ invariant mass and is equaled to $0.70 \pm 0.05$.

The Fig. 11(left) demonstrates the density of peaking background according to MC JetSet simulation after selection criteria besides "golden selection" and with $\chi^2_{4C} < 100$.

The Fig. 11(right) shows the density of peaking background after all selection reqierements. So, after $\chi^2_{4C}$ and "golden" selections the peaking $e^+e^- \to q\bar{q} \to \pi^-\pi^+\pi^0\eta$ backgrond is dominant. Evaluating the density of peaking type with obtained total normalisation factor $(0.70 \pm 0.05)$, the estimated spectrum of background $e^+e^- \to q\bar{q} \to \pi^-\pi^+\pi^0\eta$ is shown in the Fig. 12. The uncertainties in background subtraction are discussed in Sec. 4.

## 4. Background subtraction

We divide the $\pi^+\pi^-\eta$ invariant mass interval below 2.0 GeV/$c^2$ by 25 MeV/$c^2$ bins, and increase them to 50 (100) MeV/$c^2$ for region $2.0 < m_{\pi^+\pi^-\eta} < 3.1$ $(3.1 < m_{\pi^+\pi^-\eta} < 3.5)$ GeV/$c^2$ due to low statistics.

To separate signal events from the background in each bin, we subtract the peaking background using normalized MC-simulation. The peaking background consists in three following classes: 1) $e^+e^- \to q\bar{q} \to \pi^-\pi^+\pi^0\eta$ (see Fig. 12); 2) $e^+e^- \to 2\pi^\pm\pi^0\eta\gamma_{isr}$; 3) $e^+e^- \to 2K\eta\gamma_{isr}$. The density of these three types of the background is shown in the Fig. 13. The first type of peaking background is dominant.

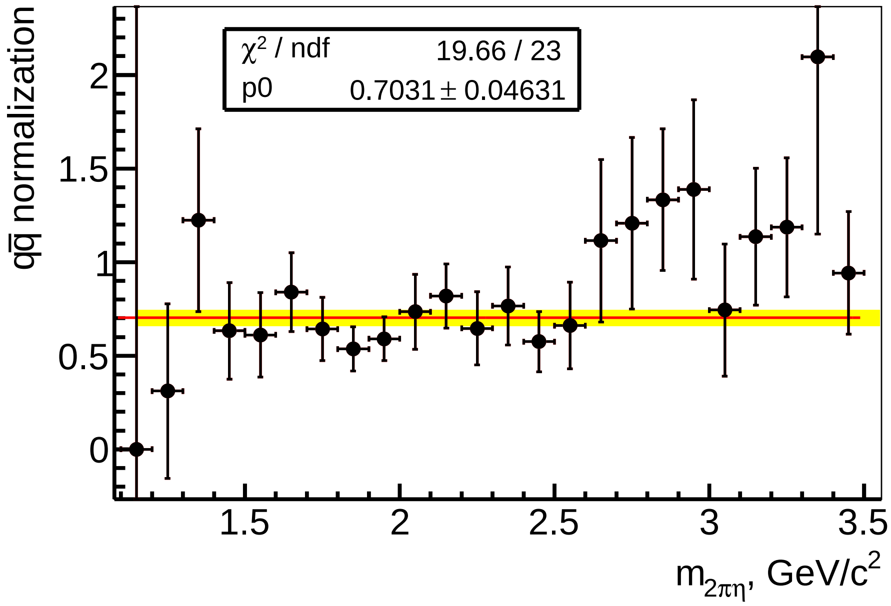

Figure 10: The $q\bar{q}$ normalization factor in the dependence of $m_{2\pi\eta}$.

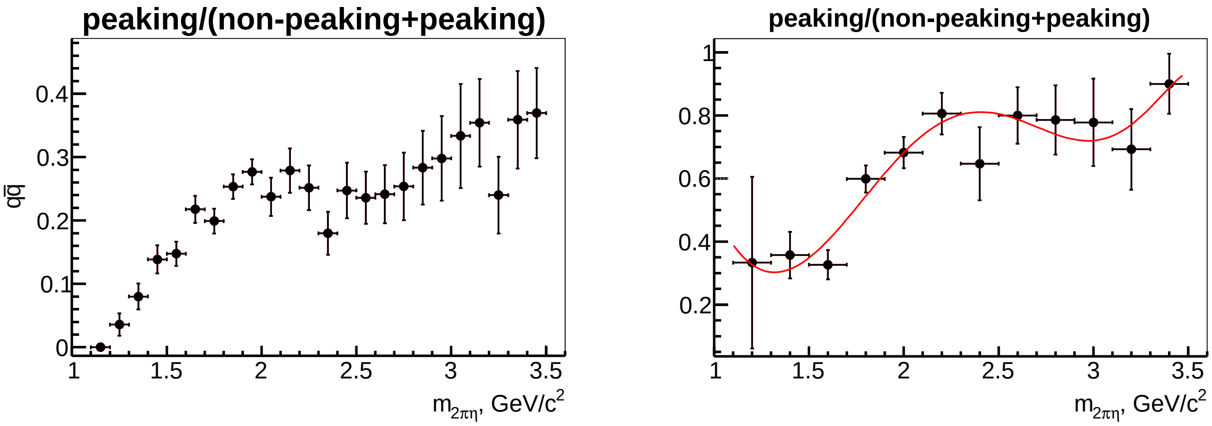

Figure 11: The density of peaking background accroding to MC JetSet simulation after preliminary selection criteria (left) and after all selection reqierements (right).

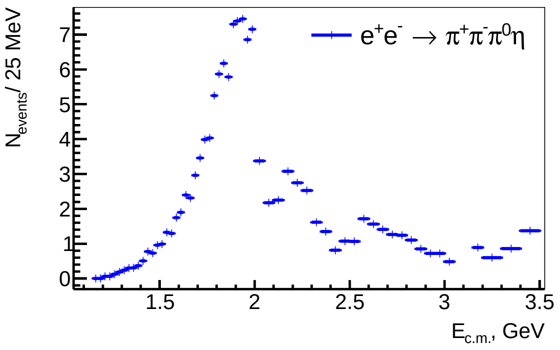

Figure 12: The estimated spectrum of peaking background $e^+e^- \to q\bar{q} \to \pi^-\pi^+\pi^0\eta$.

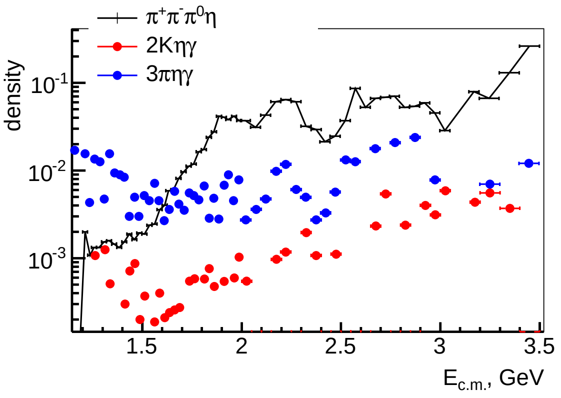

Figure 13: The density of peaking background relatively to total number of selected events.

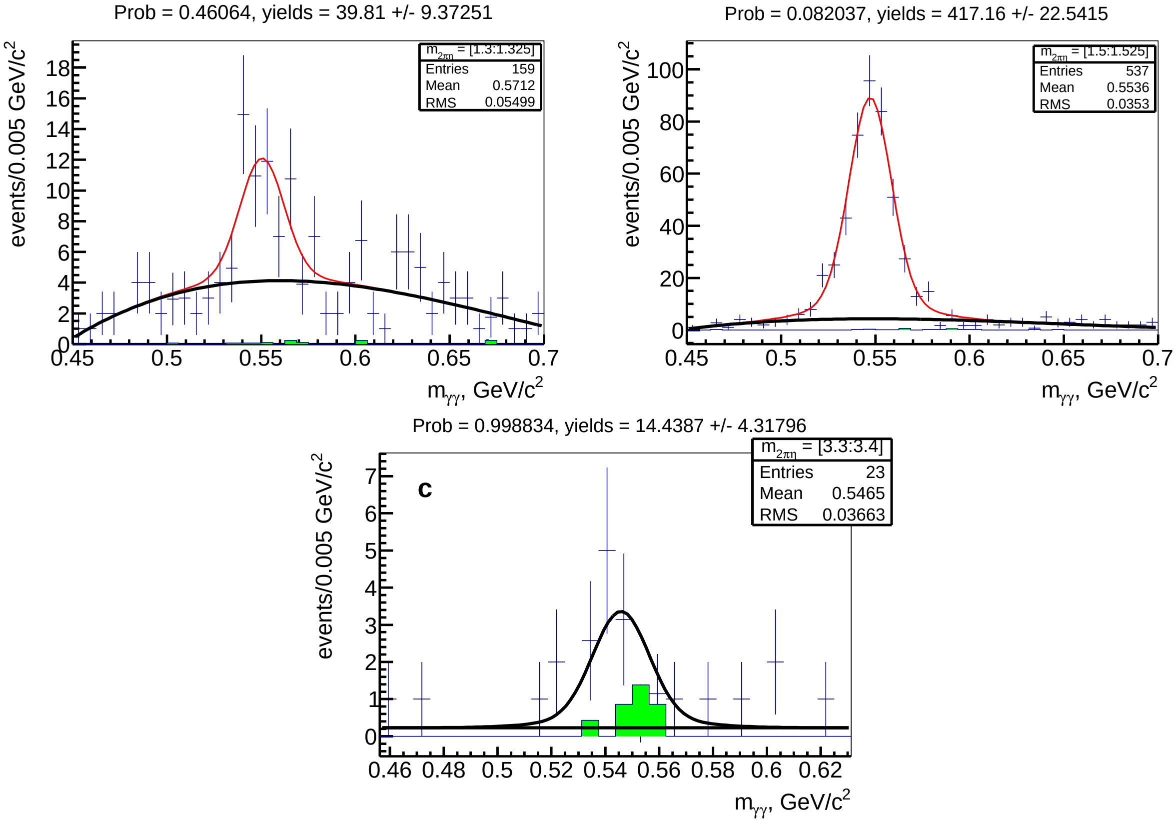

Figure 14: The approximation of two photon invariant mass for bins at $m_{\pi^+\pi^-\eta} = 1.3 \div 1.325$ GeV/$c^2$ mass interval (a), for $m_{\pi^+\pi^-\eta} = 1.5 \div 1.525$ GeV/$c^2$ (b), and for $m_{\pi^+\pi^-\eta} = 3.3 \div 3.4$ GeV/$c^2$ (c). A dashed curves correspond to the estimated background.

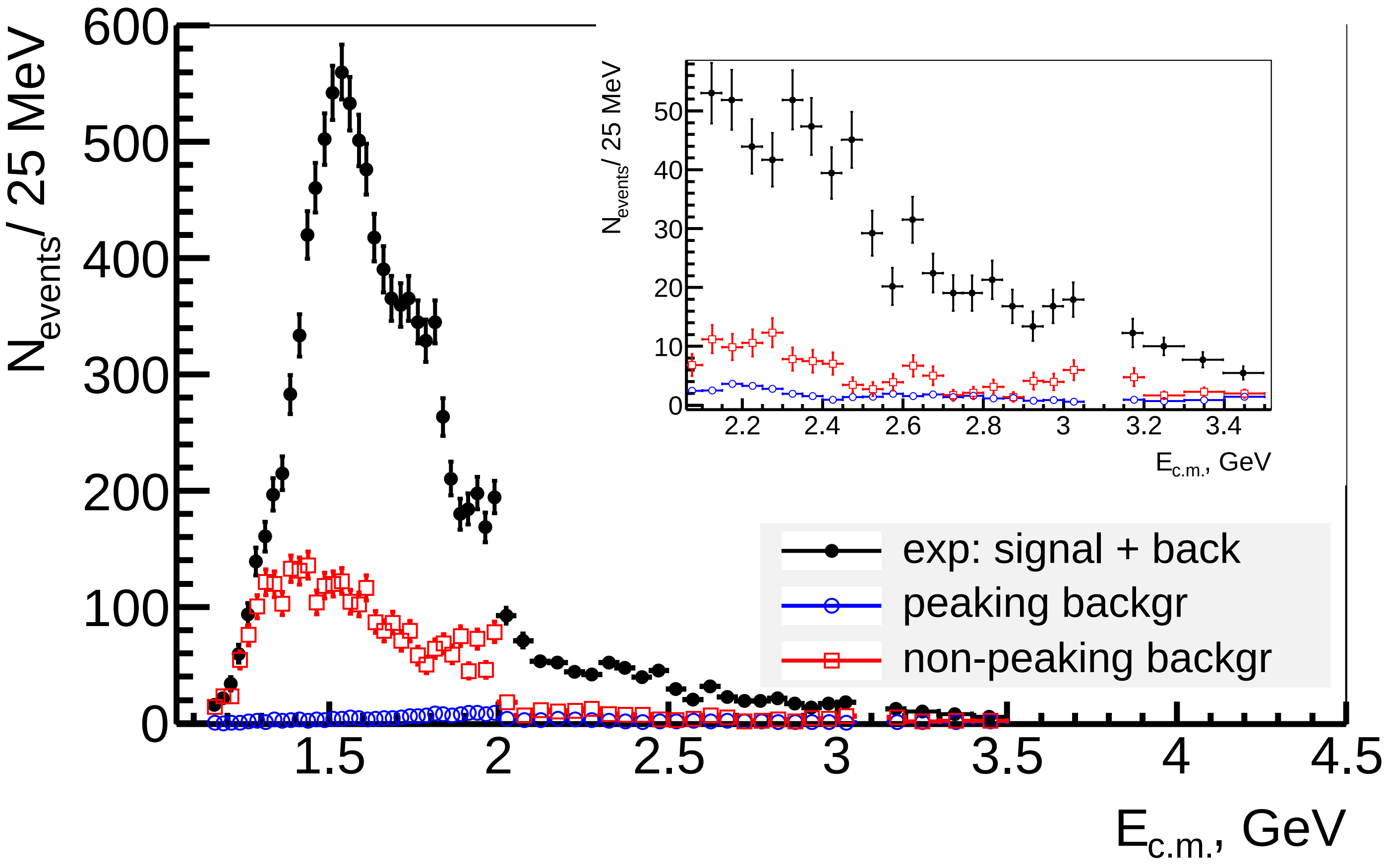

Figure 15: The $\pi^+\pi^-\eta$ invariant mass spectrum (circles) for data, and contribution of background events (squares) obtained from the $m_{\gamma\gamma}$ fit of Fig. 14. The peaked background contribution is shown by open circles.

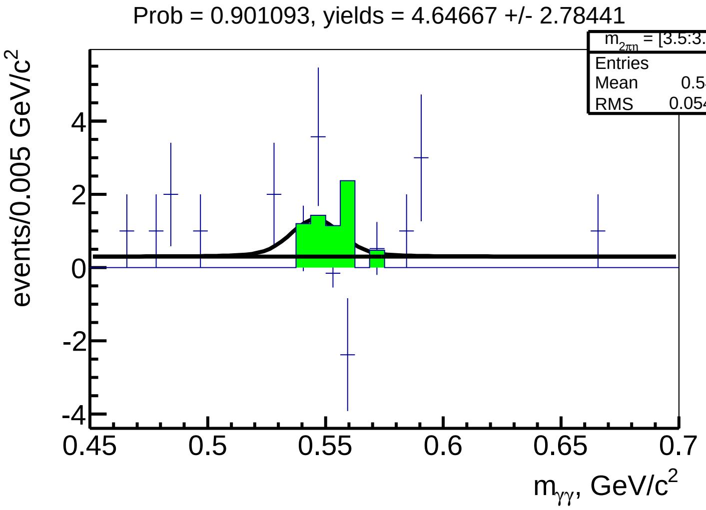

Figure 16: The two photon invariant mass distribution for $m_{2\pi\eta}$ energy region (3.5-3.6) $GeV/c^2$. Shaded histograms correspond to subtracted peaking background. Ponts with error bars is data after the subtraction.

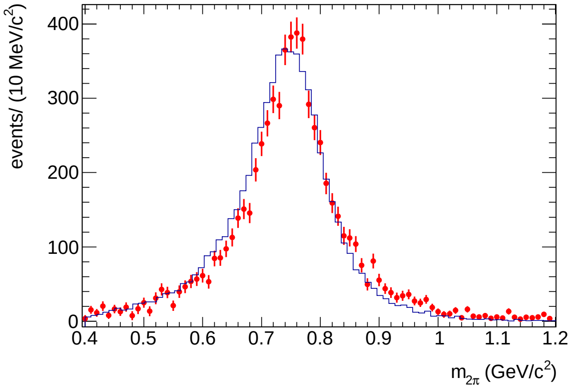

Figure 17: The two-pion invariant mass distribution for data (points with error bars) and simulated (histogramm) events from the mass range $1.4 < m_{\pi^+\pi^-\eta} < 2.0$ GeV/$c^2$.

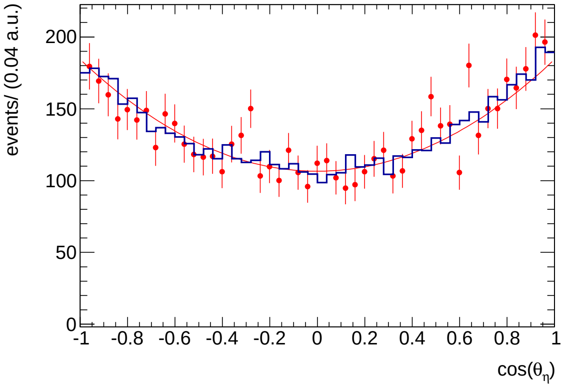

Figure 18: The $\cos\theta_\eta$ distribution for data (points with error bars) and simulated (histogramm) events from the mass range $1.4 < m_{\pi^+\pi^-\eta} < 2.0$ GeV/$c^2$. The curve is the result of the fit described in the text.

Then we fit remaining distributions with a sum of signal and a background functions. The signal function profile is described by a double-Gaussian function, parameters of which are extracted from the MC-simulation. In Region I the background profile is fixed using ISR-background simulation (predominantly $e^+e^- \to \pi^+\pi^-2\pi^0\gamma$), and is assumed to be flat in the region above 2.0 GeV/$c^2$. The examples of such fit are shown in Fig. 14 for bins at three regions of the $\pi^+\pi^-\eta$ invariant mass.

Figure 15 shows number of candidate events (circles) at each 25 MeV bin of the $\pi^+\pi^-\eta$ invariant mass. The background estimated by two photon mass approximation is illustrated by squares in Fig. 15, when circles correspond to subtracted peaked background.

For $m_{\pi^+\pi^-\eta} > 3.5$ GeV/$c^2$ the signal to background ratio becomes very small, that does not allow to perform valid signal identification (see Fig. 16).

The resulting signal mass spectrum is obtained using bin-by-bin subtraction of both backgrounds, and in studied energy range we obtain 8065.2±100.5 signal events, the numbers of peaked and non-peaked background events are 239 and 3164, respectively.

We use similar procedure of background subtraction for all other studies distributions. Figure 17 demonstrates the $\pi^+\pi^-$ invariant mass after the bin-by-bin background subtraction, in comparison with the MC-simulation for the $1.4 < m_{\pi^+\pi^-\eta} < 2.0$ GeV/$c^2$ invariant mass range. The simulated distribution is obtained using the model with the $\eta\rho(770)$ intermediate state. The observed difference between data and simulated $\pi^+\pi^-$ invariant mass distribution can be explained by the contribution of other intermediate states, for example $\eta\rho(1450)$, and its interference with the dominant $\eta\rho(770)$ amplitude. Similar effect was seen in other experiments [8],[26].

In order to estimate the effect, related with the different in MC and data $m_{2\pi}$ distributions, and its influence into detection efficiency we calculate the following ratio:

$$\delta_{model} = 1 - \frac{\int \epsilon^{reg}(m_{2\pi}) p^{exp}(m_{2\pi}) dm_{2\pi}}{\int \epsilon^{reg}(m_{2\pi}) p^{MC}(m_{2\pi}) dm_{2\pi}} = 0.004, \tag{3}$$

where $\epsilon^{reg}(m_{2\pi})$– the detection efficiency from MC in dependence on $m_{2\pi}$; $p^{MC}(m_{2\pi})$ - the two pions invariant mass distribution in MC simulation; $p^{EXP}(m_{2\pi})$ - the two pions invariant mass distribution in data.

We tried to check the discussed above effect in the MC generator level. According to Vector Dominance Model we parametrized hadronic current in the following form $e^+e^- \to V(P) \to \rho(p_1+p_2)\eta \to \pi^+(p_1)\pi^-(p_2)\eta$:

$$H_\nu = F_V(P) \cdot \epsilon_{\mu\nu\alpha\beta} \cdot P^\mu \cdot (p_1+p_2)^\alpha \cdot F_\rho(p_1+p_2) \cdot (p_1-p_2)^\beta \tag{4}$$

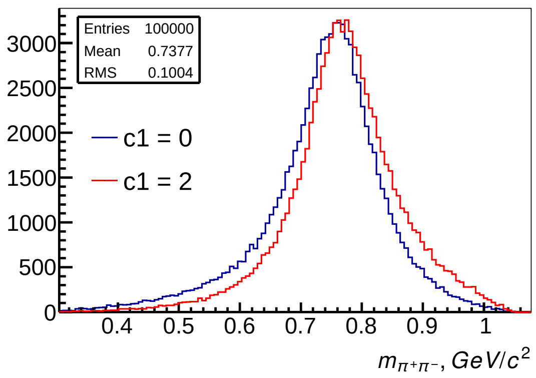

Figure 19: The MC generated invariant mass of two pions in two models which correspond to $c_1 = 0$ and $c_1 = 2$ in formula 5.

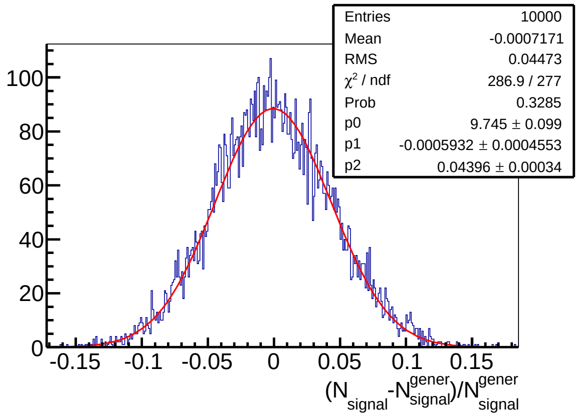

Figure 20: The relative difference of obtained and generated yields of signal as a result of toy MC procedure for the energy bin $1.35 - 1.4$ GeV/c$^2$ with 254 signal and 242 background events.

where the Form Factor of two-pion system we parametrize as:

$$F_\rho(p_1 + p_2) = \frac{m_\rho^2}{D_\rho((p_1 + p_2)^2)} + \frac{c_1 \cdot m_{\rho'}^2}{D_{\rho'}((p_1 + p_2)^2)} \tag{5}$$

The Fig. 19 demonstrate the MC generated invariant mass of two pions in two models which correspond to $c_1 = 0$ and $c_1 = 2$ in formula 5. So, the data-MC discrepancy in the Fig. 17 may be caused by $\rho'$ admixture in $\pi^+\pi^-$ origin.

Figure 18 demonstrates the cosine of the $\eta$ direction in the $\pi^+\pi^-\eta$ rest frame. We observe a reasonable agreement between data and simulation in the angular distribution. A line demonstrates a fit of data with a function $N \cdot (1 + (0.92 \pm 0.09) \cdot cos^2(\theta_\eta))$. The fit is in agreement with the expected $N \cdot (1 + cos^2(\theta_\eta))$ at the generator level.

### *4.1. Checking of background subtraction*

The possible uncertainties in background subtraction can be originated from:

1) The uncertainty in the procedure of two-photon invariant mass approximation. It is possible that used in the analysis binned likelihood fit leads to any shifts of the yields of signal events. In order to estimate the effect we perform Toy MC procedure. Using extracted from $m_{2\gamma}$ approximation signal and background profiles we generate $m_{2\gamma}$ spectrum like experimental one. Then we fit the distribution and repeat the procedure. The example of the relative difference of obtained by fit and generated yields of signal is shown in the Fig. 20. In average of the relative difference is almost not shifted from zero. It means, that the systematic uncertainty related with fit procedure is less 0.1 %.

2) The uncertainty is related with not exact knowledge of signal and background profiles used for the approximation of experimental $m_{2\gamma}$ spectrum. In order to estimate the effect we repeat the approximation of two photon invariant mass in each bin with float second polynomial function as background (besides standard procedure where we use not peaked profiles for Region I and flat profile for Region II as background spectrum). The comparison of the results is shown in the Fig. 21, that allows to estimate correspond systematic uncertainties.

3) The third error is related with peaked background subtraction. The main source of the background peaked at $\eta$ mass is the process $e^+e^- \to \pi^+\pi^-\pi^0\eta$ (see the Fig. 13). The subtraction of this background is based on the JETSET $q\bar{q}$ simulation with the normalization described in Sec. 3.1. In this subtraction, we assume that JETSET reproduces correctly the fraction of $\pi^+\pi^-\pi^0\eta$ events in the sample of $q\bar{q}$ events satisfying our selection criteria. The fraction is shown in the Fig. 11 (right) and increases from 35% to 80%. We assume that we know the fraction with the 50 % precision. The Fig. 22 shows the 50% of estimated $e^+e^- \to \pi^+\pi^-\pi^0\eta$ spectrum relatively to obtained number of signal events.

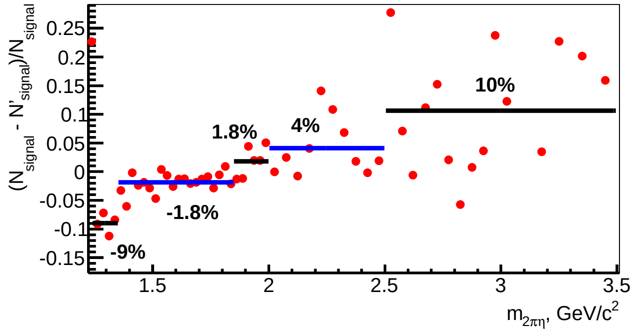

Figure 21: The relative difference of signal yields obtained by using standard background profiles ($N_{signal}$) and second polynomial function ($N'_{signal}$).

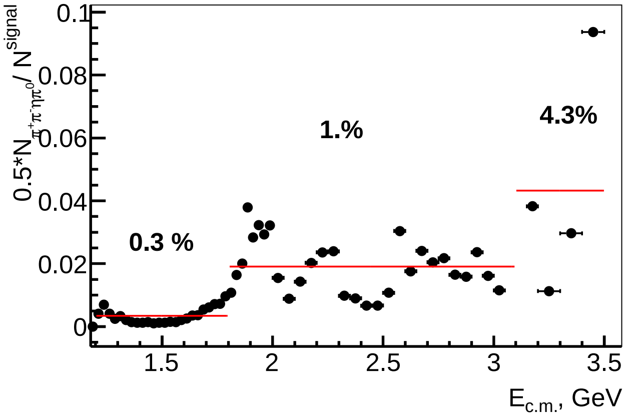

Figure 22: The 50% of estimated $e^+e^- \to \pi^+\pi^-\pi^0\eta$ spectrum relatively to obtained number of signal events.

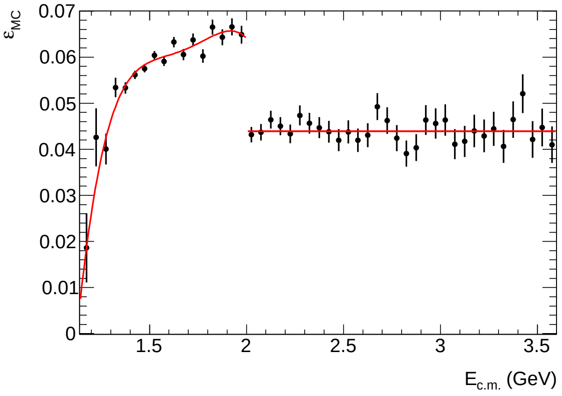

Figure 23: The reconstruction efficiency $\varepsilon_{MC}$ as a function of $m_{\pi^+\pi^-\eta}$.

Correspond uncertainty is listed in the section “Background subtraction” of Table 3.

## 5. Detection efficiency and systematic errors

A detection efficiency is defined according to:

$$\varepsilon = \varepsilon_{MC} \prod_i (1 + \delta_i), \tag{6}$$

where $\varepsilon_{MC}$ is a reconstruction efficiency, determined from MC-simulation as a ratio of the $\pi^+\pi^-\eta$ mass distribution obtained after detector response and applied selection criteria to the generated mass spectrum. The reconstruction efficiency $\varepsilon_{MC}$ as a function of $m_{\pi^+\pi^-\eta}$ is shown in Fig. 23. We introduce $\delta_i$ corrections to a different sources of a data-MC difference in the reconstruction and selection efficiency: $\chi^2_{4C}$ selection, $\eta \to \gamma\gamma$ registration efficiency, track losses, ISR photon detection efficiency, and other applied selection criteria. Also it has to be assessed how used values of selection criteria affects to detection efficiency.

### *5.1. $\chi^2_{4C}$ profile knowledge*

The $\chi^2_{4C}$ profile is not simulated exactly due to data-MC difference in the kinematic parameter resolutions, or due to NLO ISR at large polar angle ($>> 1/\gamma_{e^\pm}$), that is not included into simulation. For the $1.4 < m_{\pi^+\pi^-\eta} <$

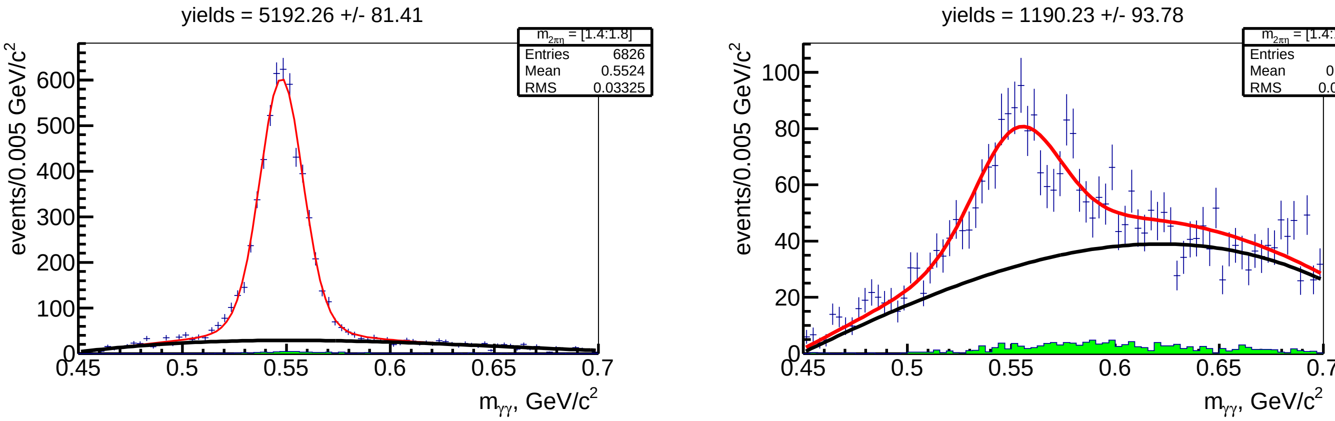

Figure 24: The approximation of two photon invariant mass in the region $1.4 < m_{\pi^+\pi^-\eta} < 1.8$ GeV/c$^2$ and requirement $\chi^2_{4C} < 25$ (left) and $25 < \chi^2_{4C} < 300$ (right). Black line corresponds to non-peaked background and shaded histogram - to peaked background contribution.

Table 2: The list of systematic uncertainties due to selection criteria.

| Selection | syst. err., % |
|---|---|
| $\chi^2_{4C} < 25(15)$ | 1.5 |
| radbhabha == 0 | 0.6 |
| kaon and muon veto | 0.4 |
| photon energy from $\eta > 0.1(0.2)$ GeV | 0.6 |
| $m^{\pi^0}_{2\gamma} > 0.16$ GeV/c$^2$ | 1.5 |
| Total error | 2.5 |

1.8 MeV/$c^2$ invariant mass region, where background contribution is relatively low, we obtain number of signal events using loose $25 < \chi^2_{4C} < 300$ selection. By compare number of events in data and MC-simulation for $\chi^2_{4C} < 25$ and $25 < \chi^2_{4C} < 300$ we obtain the following correction:

$$1 + \delta_{\chi^2<25} = \frac{N^{data}(\chi^2 < 25)}{N^{data}(25 < \chi^2 < 300) + N^{data}(\chi^2 < 25)}$$

$$\cdot \frac{N^{MC}(25 < \chi^2 < 300) + N^{MC}(\chi^2 < 25)}{N^{MC}(\chi^2 < 25)}$$

The $\delta_{\chi^2<25} = 0.4 \pm 1.5\%$ ($\delta_{\chi^2<15} = 0.6 \pm 1.3\%$) correction. We don't apply any correction for $\chi^2$ selection. The systematic uncertainty of $\chi^2$ profile knowledge is 0.5 % by variation of the background profile.

## *5.2. Remaining selections*

Influence of other selection criteria to the detection efficiency is tested by a variation of the applied parameters (see the Table 2). Relative difference of $e^+e^- \to 2\pi\eta$ cross sections obtained by using correspond requirement and without it is shown in the Fig. 25, 26, 27, 28. The shifts from zero of the histograms averages allow to estimate correspond systematic uncertainties, while the widths of the histograms are originated from statistical fluctuation of signal and backgrounds. The procedure is most sensitive to the variation of "golden" selection ($m^{\pi^0}_{2\gamma} > 0.16$ GeV/c$^2$). We do not apply any correction for that, but the observed difference is added as a systematic uncertainty in the detection efficiency, presented in Table 3 as contribution from selection criteria.

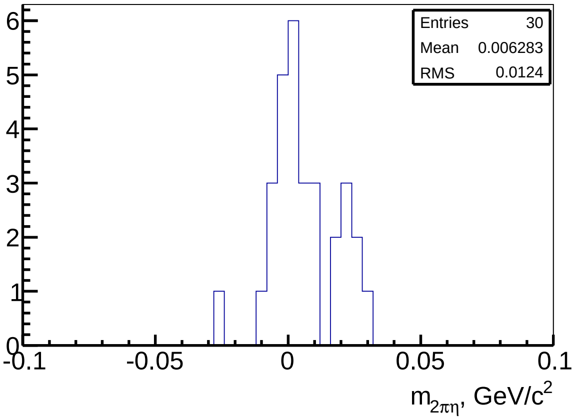

Figure 25: Relative difference of $e^+e^- \to 2\pi\eta$ cross sections obtained by using antibhabha veto requirement and without it.

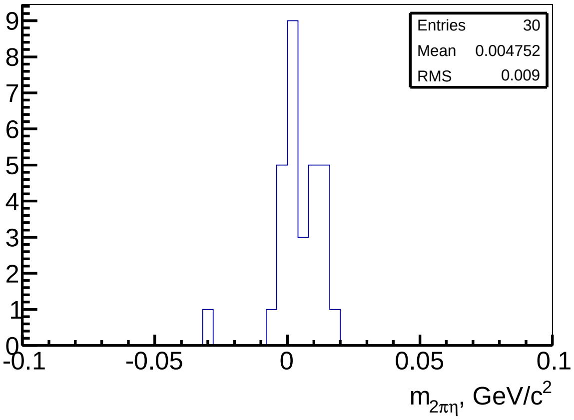

Figure 26: Relative difference of $e^+e^- \to 2\pi\eta$ cross sections obtained by using antimuon and antikaon veto requirements and without its.

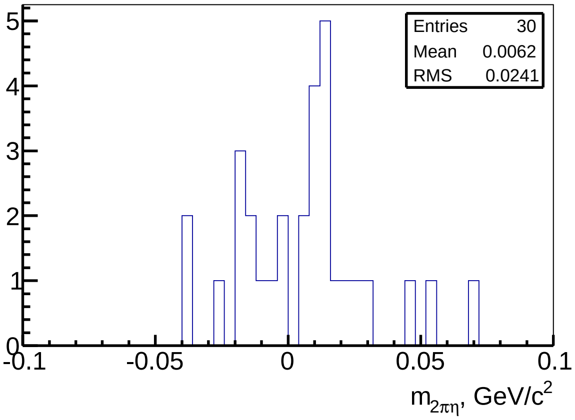

Figure 27: Relative difference of $e^+e^- \to 2\pi\eta$ cross sections obtained by using $E_{\gamma_1,\gamma_2} < 0.1$ GeV requirements and without it.

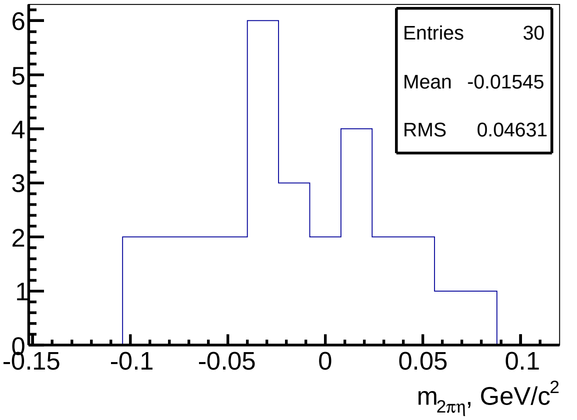

Figure 28: Relative difference of $e^+e^- \to 2\pi\eta$ cross sections obtained by using "golden" selection ($m^{\pi^0}_{2\gamma} > 0.16$ GeV/c$^2$) and without it.

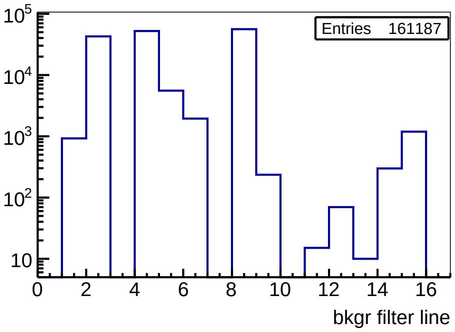

Figure 29: The distribution of BGFilter filter lines for simulated $2\pi\eta$ events.

### *5.3. triggers and filters*

We also studied the quality of the simulation of trigger and background filters used in the primary event selections. We use the overlap of the samples of events passing different filters or trigger. Collision events are reconstructed if they pass three levels of trigger. The trigger consists off hardware L1 level, online software L3 level and offline filters. Previous studies demonstrated a very low level of the L1 trigger inefficiency (few $10^{-4}$) and small discrepancy between data and simulation in L3 trigger efficiency (few $5 \cdot 10^{-3}$).

Used BGFilter lines include the following filters: "BGFMultiHadron", "BGFNeutralHadron", "BGFMuMu", "BGFTau", "BGFTwoProng", "BGFPhiGamma", "BGFAllNeutralTwoPhoton", "BGFIsr", "BGFRadTwoProng", "DigiFRadiativeBhaBha", "DigiFVirtualCompton", "DigiFDchEmcPreVeto", "DigiFL1Open", "DigiFL3Open", "BGFTwoPhotonTwoTrack". The distribution of the masks for simulated events is shown in the Fig. 29. The BGFilter inefficiency can be studied by looking a sample of events that are not required to satisfy any masks (L1 anf L3 Open). As a result $\epsilon^{MC}_{bgr.filt.} = 0.986 \pm 0.007$ and $\epsilon^{data}_{bgr.filt.} = 0.971 \pm 0.013$. And the applied efficiency correction is $1 + \delta_{trig} = 0.985 \pm 0.015$.

### *5.4. Radiative correction*

An initial state radiative correction can be determined as a ratio of visible cross section (with additional to ISR extra photon emission) to $2\pi\eta\gamma_{ISR}$ cross section. The requirement $m_{2\pi\eta\gamma_{ISR}} > 8$ GeV/c$^2$ used in simulation leads to total reduction of real and virtual parts of radiative correction closed to unity. And there is no any dependence of the correction on $2\pi\eta$ invariant mass due to identity of $d\sigma_{visible}/dq^2_{2\pi\eta\gamma_{ISR}}$ spectrums at different $m_{2\pi\eta}$ ranges (see Fig. 30). The theoretical uncertainty in the radiative emission calculation with the structure function method does't exceed 1%.

### *5.5. $\eta$ efficiency correction*

The MC simulation does't accurately reproduce merging of electromagnetic showers in BaBar calorimeters produced by photons from the $\eta$ decay and the loss of one of the decay photons.

We assume that $\eta$ efficiency correction equals to the $\pi^0$ correction at the same velocity that can be obtained from the study of $e^+e^- \to \omega\gamma_{ISR} \to \pi^0\pi^-\pi^+\gamma_{ISR}$ process.

Using detected parameters of ISR photon and charged pions $3\pi\gamma$ final state can be reconstructed performing kinematic fit with only one constrain that missing mass equals $m_{\pi^0}$ (1C fit). As a result we have $\pi^0$ candidates list with determined its energies and angles. After the checking of $\pi^0$ presence (5C fit) we extract the efficiency of $\pi^0$ registration in both data and MC simulation. The 5C fit takes into account four energy-momentum conservation equations and the requirement, that detected two-photon pair combinations have $\pi^0$ mass. Monte-Carlo simulation and data samples contains a significant contamination at low photon energy due to split-off photons associated with the charged pion tracks, additional ISR photons, FSR photons and another background depositions. Looping through all possible combinations, the one with best $\chi^2_{5C}$ value is retained. And the

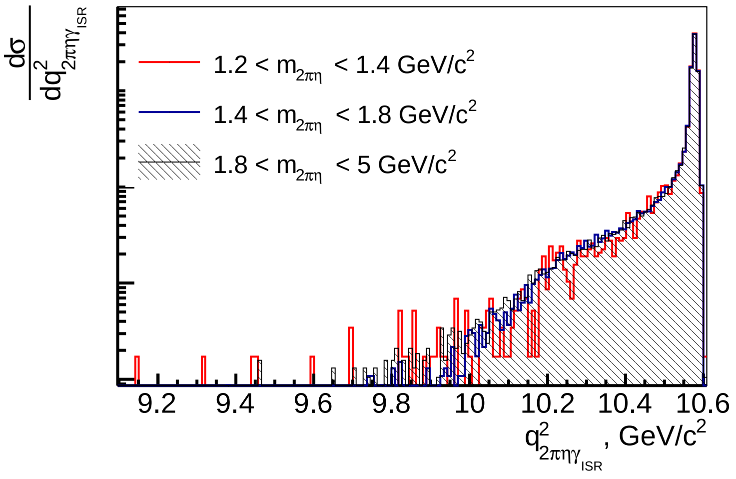

Figure 30: $d\sigma_{visible}/dq^2_{2\pi\eta\gamma_{ISR}}$ spectrums

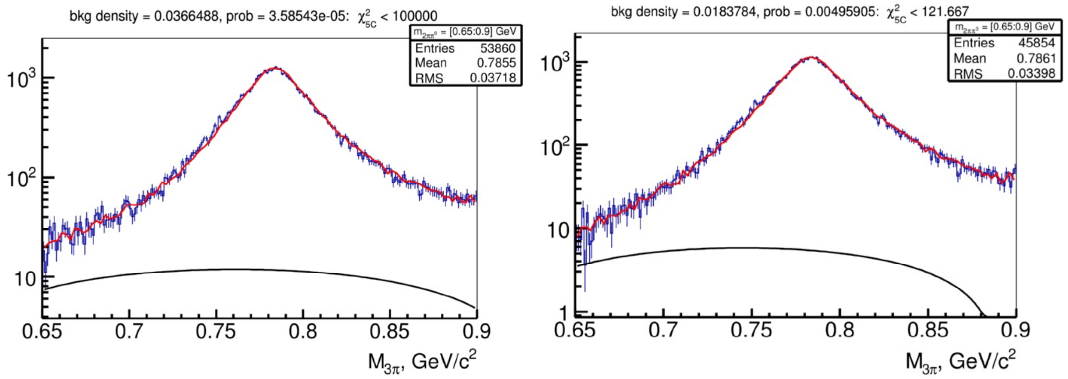

Figure 31: The $3\pi$ mass distribution for data events reconstructed without the requirement about $\pi^0$ presence (left) and after $\pi^0$ presence checking (right)

corrected after 5C fit parameters of particles are saved. The technique is described in BADs #2621, 2117 where more detailed description can be found.

The Fig. 31 demonstrates the approximation of predicted by 1C fit $3\pi$ invariant mass before $\pi^0$ presence checking (top) and after the checking (bottom). The mass spectra are fitted by a sum of distributions for signal and background events. The signal profile is extracted from simulation. The main type of background corresponds $2\pi$ and $2\pi^{\pm}2\pi^0$ production. The background has been subtracted according to simulated correspond efficiencies and cross sections. A rest background spectrum is approximated by polynomial function and approximately equals 3%.

The Fig. 32 demonstrates the dependence of the efficiency correction of $\pi^0$ registration on the applied value $\chi^2_{5C}$. The behavior can be explained by not exact description of resolution in MC simulation (before $\chi^2_{5C} = 100$) and by the simulation of extra photon emission only toward electron-positron axis. The last one leads to relatively lower values of $\chi^2_{5C}$ for events with additional hard NLO photon emission. Shown statistical error don't include correlations between different points. And the correct value of the data-MC correction may be obtained as a limit $\chi^2_{5C} \to 0$ where background contribution is negligible for both distributions in data and MC simulation.

The $\pi^0$ efficiencies and the correction $\epsilon_{data}/\epsilon_{MC}$ - 1 as a function of $\pi^0$ momentum is presented in the Fig. 33 and as a function of polar angle of $\pi^0$ - in the Fig. 34. The red points is simulation and blue - data. The average

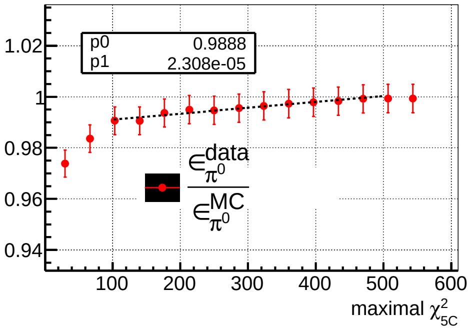

Figure 32: The dependence of obtained $\pi^0$ correction in dependence on the applied $\chi^2_{5C}$ cut.

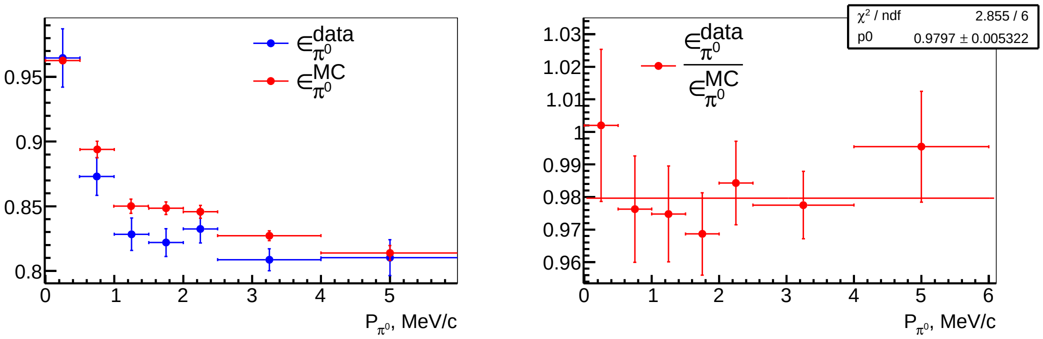

Figure 33: $\pi^0$ efficiency (a) and correspond correction (b) in dependence on $\pi^0$ momentum.

correction $\epsilon_{data}/\epsilon_{MC}$ - 1 = - 2 ± 0.5 %. It is assumed that there are no dependence on $\pi^0$ momentum and the correction can be applied also for $\eta$ correction. However, the selection criteria used for signal $e^+e^- \to 2\pi\eta\gamma$ identification differ from the ones used for $\pi^0$ efficiency calculation. In order to take possible difference we increase uncertainty and use the crrection $\delta_\eta = \epsilon_{data}/\epsilon_{MC}$ - 1 = - 2 ± 1 %.

### *5.6. tracks loss and ISR photon efficiency*

The photon spectrum from $\pi^0$ decay discussed in the previous subsection is shown in the Fig. 35. It demonstrates that the study of $\omega\gamma$ final state gives the information about photon efficiency with energy less then 1.5 GeV. The high energetic photon (> 3 GeV) efficiency was studied using the process $e^+e^- \to \mu^+\mu^-\gamma$ (BAD#1908) photon parameters can be predicted from the momenta and energies of the detected tracks of the two muons and the beam parameters. The efficiency correction as a function of polar angle was convoluted with ISR photon angle distribution of selected $2\pi\eta\gamma$ events. The distributions before and after convolution are shown in the Fig. 36. As a result the correction $\delta_{\gamma_{ISR}} = -1.1 \pm 1\%$ was applied.

The correction due to the no exact simulation of track loss is used from the study $2\pi^+2\pi^-\gamma$ final state (BAD#2079, 2370). Here it was found that tracking inefficiency per track including track overlap is:

$\eta_{data} - \eta_{MC} = \delta\eta = (0.75 \pm 0.05_{stat} \pm 0.34_{syst})\%$.

Deleting the effect due to track overlap with opposite tracks (the effect of same charge track overlapping is well modelled in MC) the efficiency difference between data and simulation of:

$\eta'_{data} - \eta'_{MC} = \delta\eta' = (0.38 \pm 0.05_{stat} \pm 0.39_{syst})\%$.

It should be mentioned that $2\pi^+2\pi^-\gamma$ events sample includes the possibility for each track of overlapping with two opposite tracks besides $2\pi\eta\gamma$ system.

So, data-MC correction for $\pi^+$ and $\pi^-$ for $2\pi\eta\gamma$ system can be estimated as:

$\delta_{track} = \frac{\epsilon_{exp}}{\epsilon_{mc}} - 1 = -2 \times (\delta\eta' + 0.5(\delta\eta - \delta\eta')) = -1.1 \pm 0.5$

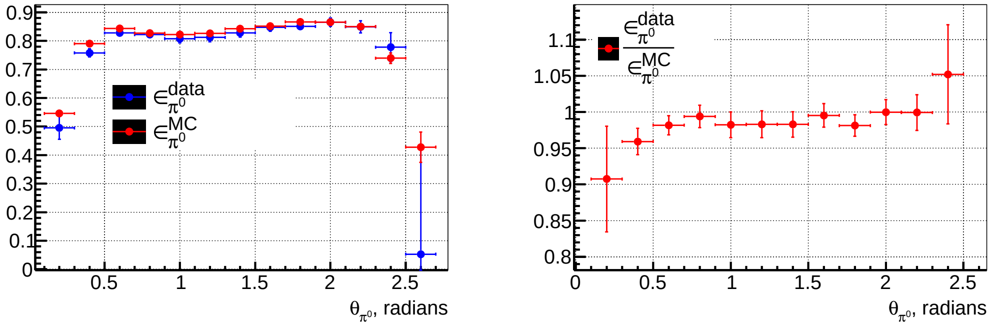

Figure 34: $\pi^0$ efficiency (a) and correspond correction (b) in dependence on $\pi^0$ polar angle.

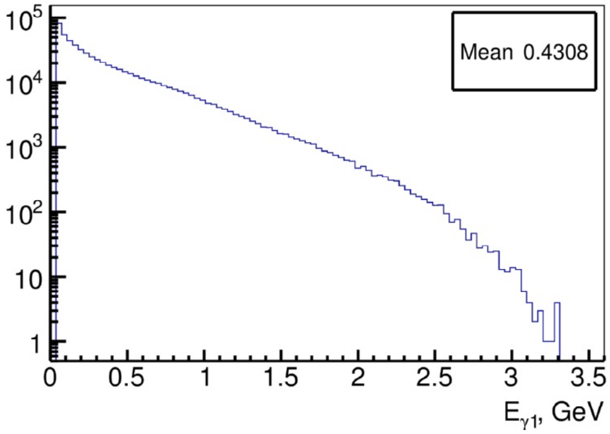

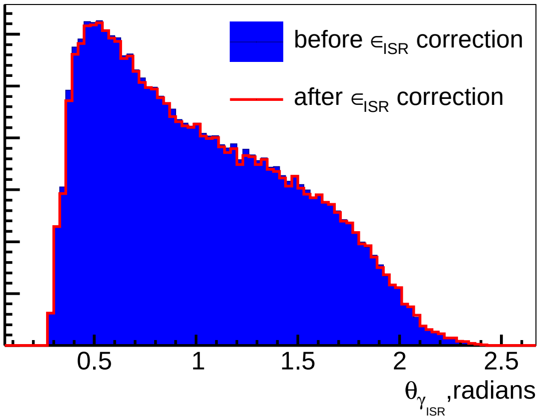

Figure 35: The photon spectrum from $\pi^0$ decay used for $\pi^0$ efficiency study

Figure 36: The ISR photon polar angle distribution of selected $2\pi\eta\gamma$ events before and after efficiency correction.

Table 3: Summary of the efficiency corrections and systematic uncertainties.

| Source | Correction, % | Systematic uncertainty, % |
|---|---|---|
| Selection criteria | | 2.5 |
| Background subtraction | | |
| $m_{\pi^+\pi^-\eta} < 1.35$ | | 9 |
| $1.35 < m_{\pi^+\pi^-\eta} < 1.80$ | | 2 |
| $1.80 < m_{\pi^+\pi^-\eta} < 2.50$ | | 5 |
| $2.50 < m_{\pi^+\pi^-\eta} < 3.10$ | | 10.5 |
| $3.10 < m_{\pi^+\pi^-\eta} < 3.50$ | | 11 |
| $\eta$ reconstruction | -2 | 1.0 |
| Track reconstruction | -1.1 | 1.0 |
| ISR photon efficiency | -1.1 | 1.0 |
| Trigger and filters | -1.5 | 1.6 |
| Radiative correction | | 1.0 |
| Luminosity | | 1.0 |
| Total | | |
| $m_{\pi^+\pi^-\eta} < 1.35$ | -5.7 | 10 |
| $1.35 < m_{\pi^+\pi^-\eta} < 1.80$ | -5.7 | 4.5 |
| $1.80 < m_{\pi^+\pi^-\eta} < 2.50$ | -5.7 | 6.5 |
| $2.50 < m_{\pi^+\pi^-\eta} < 3.10$ | -5.7 | 11 |
| $3.10 < m_{\pi^+\pi^-\eta} < 3.50$ | -5.7 | 12 |

And increasing the systematic error to account for the possible dependence of the correction on track multiplicity and track momenta the correction $\delta_{track} = -1.1 \pm 1\%$ was apllied.

All efficiency corrections and errors, dicsussed in this section, are summarized in the Table 3. The overall correction to detection efficiency is -5.7%, and estimated systematic uncertainty is 4.5% in the $1.35 < m_{\pi^+\pi^-\eta} < 1.8$ GeV/$c^2$ invariant mass region, and increases to 12% at the end of studied mass interval.

## 6. THE $e^+e^- \to \pi^+\pi^-\eta$ cross section calculation

Using the $\pi^+\pi^-\eta$ mass spectrum of the signal events we calculate Born cross section $\sigma(E_{\text{c.m.}})$ as:

$$\sigma_{\pi^+\pi^-\eta}(E_{\text{c.m.}}) = \frac{(dN/dm)_{corr}}{dL/dm \cdot \varepsilon(m) \cdot R}, \tag{7}$$

where $E_{\text{c.m.}} = m$ - invariant mass of $\pi^+\pi^-\eta$ system; $(dN/dm)_{corr}$ is the $\pi^+\pi^-\eta$ mass spectrum after correction on detector resolution (unfolding); $dL/dm$ is so-called ISR differential luminosity [26]; $\varepsilon(m)$ is the detection efficiency; $R$ is a initial state radiative correction factor close to unity in our case with theoretical uncertainty less than 1%. Systematic uncertainties in $dL/dm$ and $R$ are added to Table 3, and together with other errors contribute to total systematic error of the cross section.

Number of events in each bin $i$ of Fig. 15 is related to "true" number as $dN(i) = \sum A(i,j) \cdot dN_{corr}(j)$, where $A(i,j)$ is a migration matrix, describing a probability of "true" event in bin $j$ contribute to bin $i$. The matrix $A(i,j)$ is extracted from the simulation and slightly depends on energy. The distribution of the difference between measured and true $\pi^+\pi^-\eta$ mass for simulated events with correspond selection criteria from the mass Region I is shown in Fig. 38. The curve is a fit to a double-Gaussian function which is used to calculate the migration matrix $A(i,j)$. For the 25 MeV bin width the diagonal elements are $A(i,i) \approx 0.83$, and next to diagonal elements are $A(i \pm 1, i) \approx 0.08$.

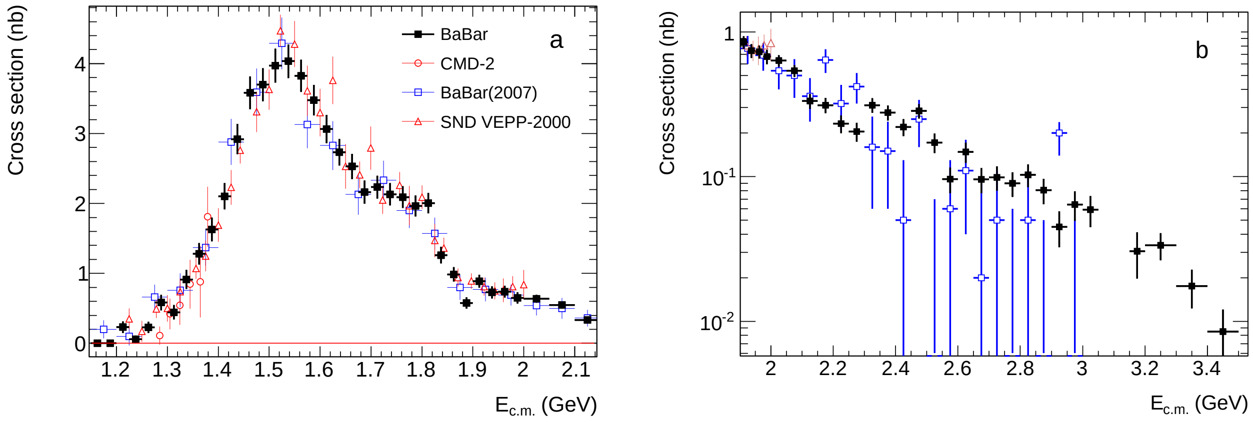

Figure 37: Cross section of the process $e^+e^- \to \pi^+\pi^-\eta$ as a function of $E_{\text{c.m.}}$ for Region I (a), and Region II (b).

Table 4: Results of the $e^+e^- \to \pi^+\pi^-\eta$ reaction study: The c.m. energy range ($E_{\text{c.m.}}$), number of selected events after $\pi^+\pi^-\eta$-mass-resolution ($N_{\text{corr}}$), detection efficiency ($\varepsilon$), differential ISR luminosity ($L$), and measured cross section ($\sigma$). The systematic uncertainty on the cross section in different energy intervals is listed in Table 3.

| $E_{\text{c.m.}}$, GeV | $N_{\text{corr}}$ | $\varepsilon$, % | L, $\text{nb}^{-1}$ | $\sigma$, nb |
|---|---|---|---|---|
| 1.150 - 1.175 | < 1 (90% C.L.) | 1.36 | 1439 | < 0.05 (90% C.L.) |
| 1.175 - 1.20 | < 1 (90% C.L.) | 2.12 | 1468 | < 0.03 (90% C.L.) |
| 1.20 - 1.225 | 9 ± 3 | 2.77 | 1497 | 0.231 ± 0.083 |
| 1.225 - 1.250 | 2 ± 2 | 3.33 | 1528 | 0.058 ± 0.052 |
| 1.250 - 1.275 | 13 ± 4 | 3.79 | 1558 | 0.228 ± 0.081 |
| 1.275 - 1.300 | 38 ± 7 | 4.18 | 1589 | 0.583 ± 0.112 |
| 1.300 - 1.325 | 32 ± 7 | 4.51 | 1621 | 0.444 ± 0.103 |
| 1.325 - 1.350 | 72 ± 10 | 4.77 | 1652 | 0.914 ± 0.134 |
| 1.350 - 1.375 | 107 ± 12 | 4.98 | 1685 | 1.280 ± 0.154 |
| 1.375 - 1.40 | 144 ± 15 | 5.15 | 1717 | 1.628 ± 0.170 |
| 1.400 - 1.425 | 195 ± 17 | 5.28 | 1750 | 2.103 ± 0.189 |
| 1.425 - 1.450 | 281 ± 20 | 5.38 | 1783 | 2.920 ± 0.216 |
| 1.450 - 1.475 | 357 ± 23 | 5.46 | 1817 | 3.582 ± 0.235 |
| 1.475 - 1.500 | 380 ± 24 | 5.53 | 1851 | 3.699 ± 0.237 |
| 1.500 - 1.525 | 419 ± 25 | 5.57 | 1885 | 3.970 ± 0.241 |
| 1.525 - 1.550 | 436 ± 26 | 5.61 | 1920 | 4.035 ± 0.240 |
| 1.550 - 1.575 | 424 ± 25 | 5.65 | 1955 | 3.826 ± 0.231 |
| 1.575 - 1.600 | 394 ± 24 | 5.68 | 1990 | 3.476 ± 0.218 |
| 1.600 - 1.625 | 355 ± 23 | 5.71 | 2025 | 3.065 ± 0.203 |
| 1.625 - 1.650 | 324 ± 22 | 5.74 | 2061 | 2.732 ± 0.189 |
| 1.650 - 1.675 | 307 ± 21 | 5.78 | 2097 | 2.528 ± 0.179 |
| 1.675 - 1.700 | 269 ± 20 | 5.82 | 2133 | 2.161 ± 0.166 |
| 1.700 - 1.725 | 285 ± 21 | 5.86 | 2170 | 2.233 ± 0.164 |
| 1.725 - 1.750 | 278 ± 20 | 5.91 | 2206 | 2.130 ± 0.159 |
| 1.750 - 1.775 | 280 ± 20 | 5.96 | 2243 | 2.091 ± 0.155 |
| 1.775 - 1.800 | 270 ± 20 | 6.01 | 2280 | 1.965 ± 0.149 |
| 1.800 - 1.825 | 282 ± 20 | 6.06 | 2317 | 2.005 ± 0.146 |
| 1.825 - 1.850 | 182 ± 17 | 6.11 | 2355 | 1.262 ± 0.118 |
| 1.850 - 1.875 | 145 ± 15 | 6.15 | 2392 | 0.987 ± 0.101 |
| 1.875 - 1.900 | 86 ± 12 | 6.17 | 2430 | 0.575 ± 0.081 |
| 1.875 - 1.900 | 86 ± 12 | 6.17 | 2430 | 0.575 ± 0.081 |
| 1.900 - 1.925 | 136 ± 14 | 6.19 | 2468 | 0.888 ± 0.092 |
| 1.925 - 1.950 | 113 ± 13 | 6.18 | 2506 | 0.728 ± 0.086 |
| 1.950 - 1.975 | 115 ± 13 | 6.15 | 2545 | 0.736 ± 0.085 |
| 1.975 - 2.00 | 102 ± 12 | 6.08 | 2583 | 0.648 ± 0.081 |
| 2.00 - 2.05 | 138 ± 12 | 4.14 | 5283 | 0.632 ± 0.057 |
| 2.05 - 2.10 | 122 ± 11 | 4.14 | 5439 | 0.544 ± 0.050 |
| 2.10 - 2.15 | 78 ± 9 | 4.14 | 5596 | 0.337 ± 0.039 |
| 2.15 - 2.20 | 76 ± 9 | 4.14 | 5754 | 0.317 ± 0.038 |
| 2.20 - 2.25 | 58 ± 8 | 4.14 | 5914 | 0.236 ± 0.033 |
| 2.25 - 2.30 | 52 ± 7 | 4.14 | 6074 | 0.209 ± 0.031 |
| 2.30 - 2.35 | 82 ± 9 | 4.14 | 6236 | 0.317 ± 0.036 |
| 2.35 - 2.40 | 74 ± 9 | 4.14 | 6399 | 0.281 ± 0.033 |
| 2.40 - 2.45 | 60 ± 8 | 4.14 | 6564 | 0.223 ± 0.030 |
| 2.45 - 2.50 | 80 ± 9 | 4.14 | 6729 | 0.287 ± 0.032 |
| 2.50 - 2.55 | 49 ± 7 | 4.14 | 6896 | 0.173 ± 0.026 |
| 2.55 - 2.60 | 28 ± 5 | 4.14 | 7065 | 0.096 ± 0.019 |
| 2.60 - 2.65 | 44 ± 7 | 4.14 | 7235 | 0.147 ± 0.023 |
| 2.65 - 2.70 | 29 ± 5 | 4.14 | 7407 | 0.095 ± 0.018 |
| 2.70 - 2.75 | 30 ± 5 | 4.14 | 7581 | 0.097 ± 0.018 |
| 2.75 - 2.80 | 28 ± 5 | 4.14 | 7756 | 0.088 ± 0.017 |
| 2.80 - 2.85 | 33 ± 6 | 4.14 | 7933 | 0.101 ± 0.018 |
| 2.85 - 2.90 | 26 ± 5 | 4.14 | 8113 | 0.079 ± 0.015 |
| 2.90 - 2.95 | 15 ± 4 | 4.14 | 8294 | 0.044 ± 0.012 |
| 2.95 - 3.00 | 22 ± 5 | 4.14 | 8478 | 0.063 ± 0.014 |
| 3.00 - 3.05 | 20 ± 5 | 4.14 | 8665 | 0.058 ± 0.014 |
| 3.15 - 3.20 | 11 ± 4 | 4.14 | 9241 | 0.030 ± 0.010 |
| 3.20 - 3.30 | 26 ± 5 | 4.14 | 19077 | 0.033 ± 0.007 |
| 3.30 - 3.40 | 14 ± 4 | 4.14 | 19893 | 0.017 ± 0.005 |
| 3.40 - 3.50 | 7 ± 3 | 4.14 | 20737 | 0.008 ± 0.003 |

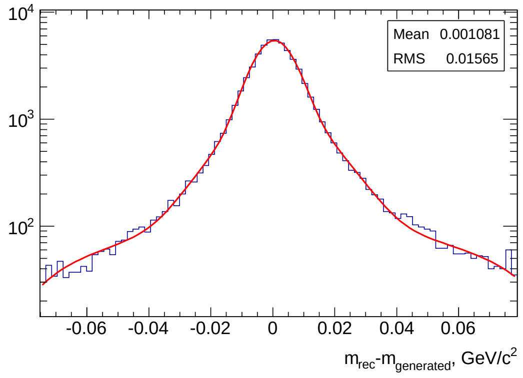

Figure 38: The distribution of the difference between measured and true $\pi^+\pi^-\eta$ mass for simulated events with correspond selection criteria from the mass Region I. The curve is a fit to a double-Gaussian function.

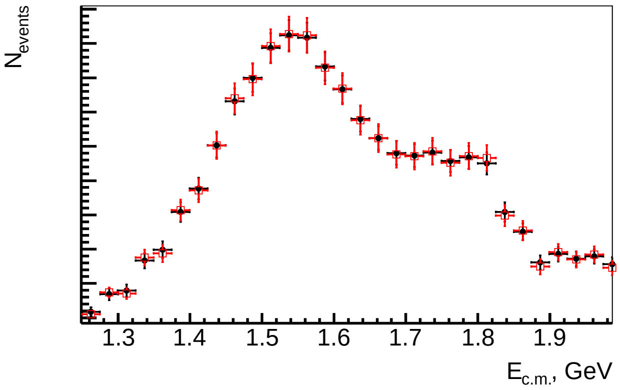

Figure 39: The spectrums before (circles) $(dN/dm)$ and after (squares) unfolding $(dN/dm)_{corr}$.

In more details, A =

$$\begin{pmatrix}
0.825 & 0.083 & 0.003 & 0 & 0 & 0 & 0 & 0 & 0 & 0\cdots \\
0.083 & 0.825 & 0.083 & 0.003 & 0 & 0 & 0 & 0 & 0 & 0\cdots \\
0.003 & 0.083 & 0.825 & 0.083 & 0.003 & 0 & 0 & 0 & 0 & 0\cdots \\
0 & 0.003 & 0.083 & 0.825 & 0.083 & 0.003 & 0 & 0 & 0 & 0\cdots \\
0 & 0 & 0.003 & 0.083 & 0.825 & 0.083 & 0.003 & 0 & 0 & 0\cdots \\
0 & 0 & 0 & 0.003 & 0.083 & 0.825 & 0.083 & 0.003 & 0 & 0\cdots \\
0 & 0 & 0 & 0 & 0.003 & 0.083 & 0.825 & 0.083 & 0.003 & 0\cdots \\
0 & 0 & 0 & 0 & 0 & 0.003 & 0.083 & 0.825 & 0.083 & 0.003\cdots \\
0 & 0 & 0 & 0 & 0 & 0 & 0.003 & 0.083 & 0.825 & 0.083\cdots \\
0 & 0 & 0 & 0 & 0 & 0 & 0 & 0.003 & 0.083 & 0.825\cdots \\
\cdots & \cdots & \cdots & \cdots & \cdots & \cdots & \cdots & \cdots & \cdots & \cdots
\end{pmatrix}$$

Using the most general (Gauss-Jordan) matrix inverse algorithm, implemented into ROOT (TMatrixD Invert(double *)) [29], we obtain matrix as following: $A^{-1}$=

$$\begin{pmatrix}
1.223 & -0.124 & 0.007 & 0 & 0 & 0 & 0 & 0 & 0 & 0\cdots \\
-0.124 & 1.236 & -0.125 & 0.007 & 0 & 0 & 0 & 0 & 0 & 0\cdots \\
0.007 & -0.125 & 1.236 & -0.125 & 0.007 & 0 & 0 & 0 & 0 & 0\cdots \\
0 & 0.007 & -0.125 & 1.236 & -0.125 & 0.007 & 0 & 0 & 0 & 0\cdots \\
0 & 0 & 0.007 & -0.125 & 1.236 & -0.125 & 0.007 & 0 & 0 & 0\cdots \\
0 & 0 & 0 & 0.007 & -0.125 & 1.236 & -0.125 & 0.007 & 0 & 0\cdots \\
0 & 0 & 0 & 0 & 0.007 & -0.125 & 1.236 & -0.125 & 0.007 & 0\cdots \\
0 & 0 & 0 & 0 & 0 & 0.007 & -0.125 & 1.236 & -0.125 & 0.007\cdots \\
0 & 0 & 0 & 0 & 0 & 0 & 0.007 & -0.125 & 1.236 & -0.125\cdots \\
0 & 0 & 0 & 0 & 0 & 0 & 0 & 0.007 & -0.125 & 1.236\cdots \\
\cdots & \cdots & \cdots & \cdots & \cdots & \cdots & \cdots & \cdots & \cdots & \cdots
\end{pmatrix}$$

The inverse of this migration matrix is applied to the measured spectrum, and $(dN/dm)_{corr}$ is used in the cross section calculation.

$$\begin{gathered}
\mathrm{dN}_{corr}(i) = \sum A^{-1}(i,j)\cdot dN(j) \\
\sigma(dN_{corr}(i)) = \sqrt{\sum (A^{-1}(i,j)\cdot \sigma(dN(j)))^2}
\end{gathered} \tag{8}$$

Fig. 39 and Table 5 contains the comparison of the spectrums $(dN/dm)$ and $(dN/dm)_{corr}$. Due to absence of a narrow structure in the spectrum, the correction is found to be not very significant in comparison with statistic uncertainties, but leads to an increase in the errors (by 4-15%) and their correlation. However, the unfolding procedure gives a relatively large correction, about -8%, for the energy bin $1.8875 < m_{\pi^+\pi^-\eta} < 1.900$ MeV/$c^2$.

Table 4 contains the results of the cross section calculation in the energy range $E_{\mathrm{c.m.}} = 1.15 \div 3.5$ GeV, and the cross section is shown in Fig. 37 in comparison with other measurements. The uncertainty of the presented cross section contains only diagonal statistic uncertainties.

In order to perform a complete calculation of statistical errors we calculate the correlation matrix according to following:

Table 5: The number of events in mass bins before ($N$) and after resolution correction ($N_{corr}$).

| $\sqrt{s}$, GeV | $dN/dm$ | $(dN/dm)_{corr}$ |
|---|---|---|
| 1.2 - 1.225 | 7.8978 ± 4.38387 | 9.66185 ±3.47885 |
| 1.225 - 1.25 | 4.53053 ± 5.30536 | 2.98849 ±2.69964 |
| 1.25 - 1.275 | 14.8622 ± 6.79058 | 13.5715 ±4.83424 |
| 1.275 - 1.3 | 36.2814 ± 8.71999 | 38.9448 ±7.50258 |
| 1.3 - 1.325 | 36.651 ± 9.19583 | 32.5989 ±7.59965 |
| 1.325 - 1.35 | 72.1239 ± 11.1078 | 72.3387 ±10.6097 |
| 1.35 - 1.375 | 108.049 ± 12.7077 | 107.91 ±12.9867 |
| 1.375 - 1.4 | 146.01 ± 14.6023 | 144.614 ±15.1029 |
| 1.4 - 1.425 | 198.56 ± 16.6054 | 195.313 ±17.6166 |
| 1.425 - 1.45 | 280.682 ± 19.1505 | 281.718 ±20.9253 |
| 1.45 - 1.475 | 352.526 ± 20.5847 | 357.284 ±23.4407 |
| 1.475 - 1.5 | 381.287 ± 21.5836 | 380.06 ±24.3956 |
| 1.5 - 1.525 | 417.16 ± 22.5415 | 419.147 ±25.5091 |
| 1.525 - 1.55 | 433.908 ± 22.9518 | 436.768 ±26.0136 |
| 1.55 - 1.575 | 422.52 ± 22.6286 | 424.203 ±25.673 |
| 1.575 - 1.6 | 393.642 ± 21.6575 | 394.462 ±24.7828 |
| 1.6 - 1.625 | 356.661 ± 21.0982 | 355.979 ±23.5946 |
| 1.625 - 1.65 | 326.003 ± 19.8504 | 324.77 ±22.5595 |
| 1.65 - 1.675 | 305.957 ± 19.1473 | 307.642 ±21.847 |
| 1.675 - 1.7 | 274.048 ± 18.5332 | 269.271 ±20.6963 |
| 1.7 - 1.725 | 283.435 ± 18.5898 | 285.238 ±21.0266 |
| 1.725 - 1.75 | 279.514 ± 18.5731 | 278.887 ±20.8872 |
| 1.75 - 1.775 | 279.714 ± 18.1042 | 280.701 ±20.8901 |
| 1.775 - 1.8 | 272.06 ± 18.0145 | 270.437 ±20.6084 |
| 1.8 - 1.825 | 272.843 ± 18.2127 | 282.765 ±20.6018 |
| 1.825 - 1.85 | 187.573 ± 15.4288 | 182.233 ±17.1286 |
| 1.85 - 1.875 | 144.286 ± 13.6053 | 145.73 ±15.0035 |
| 1.875 - 1.9 | 96.264 ± 11.9321 | 86.764 ±12.3097 |
| 1.9 - 1.925 | 130.144 ± 13.0889 | 136.237 ±14.2244 |
| 1.925 - 1.95 | 115.352 ± 12.6216 | 113.36 ±13.4253 |
| 1.95 - 1.975 | 114.597 ± 11.9057 | 115.766 ±13.368 |
| 1.975 - 2 | 106.813 ± 12.2944 | 102.386 ±12.8134 |

$$\begin{gathered}
N = AN_0 \\
\mathrm{cov}_{i,j} = \overline{(N_{0i} - \overline{N_{0i}})((N_{0j} - \overline{N_{0j}})} = \overline{N_{0i}N_{0j}} - \bar{N_{0i}}\bar{N_{0j}} = \\
= \sum_{l,k} A^{-1}_{il} A^{-1}_{jk} (\overline{N_k N_l} - \bar{N}_k \bar{N}_l) \text{—only elements with k=l are not equal 0—} = \\
= \sum_l A^{-1}_{il} A^{-1}_{jl} \sigma_l^2 \\
\mathrm{corr}_{i,j} = \rho_{i,j} = \frac{cov_{i,j}}{\sqrt{cov_{i,i}}\sqrt{cov_{j,j}}}
\end{gathered} \tag{9}$$

As a result we obtain the values $\rho_{i,i\pm1} \approx -0.20$, $\rho_{i,i\pm2} \approx 0.02$, $\rho_{i,i\pm3} \approx 0.002$. The values should be used in order to calculate the total uncertainty of a quantity, calculation of which depends on cross section values. So,

$$\begin{gathered}
\mathrm{f} = \mathrm{f}(\sigma_1, \sigma_2, \sigma_i, ...) \\
\sigma_f^2 = \sum\sum \rho_{i,j} \frac{df}{d\sigma_i}\frac{df}{d\sigma_j} \sigma(\sigma_i)\sigma(\sigma_j),
\end{gathered} \tag{10}$$

where $\rho_{i,j}$ - correlation coefficients, $\sigma(\sigma_i)$ - standart deviation of cross section in the bin number i.

## 7. FIT TO THE $e^+e^- \to \pi^+\pi^-\eta$ cross section

In the framework of the VMD model the $e^+e^- \to \pi^+\pi^-\eta$ cross section is described by a sum of the contributions of the isovector states $\rho(770)$, $\rho(1450)$, $\rho(1700)$, $\rho'''$, etc., decaying to $\eta\rho(770) \to \eta\pi^+\pi^-$ [10]:

$$\sigma(s) = \frac{4\alpha^2}{3}\frac{1}{s\sqrt{s}}|F(s)|^2 G(s),\ \ G(s) = \int_{4m_\pi^2}^{(\sqrt{s}-m_\eta)^2} dq^2 \frac{\sqrt{q^2}\Gamma_\rho(q^2)p_\eta^3(s,q^2)}{(q^2-m_\rho^2)^2 + (\sqrt{q^2}\Gamma_\rho(q^2))^2}, \tag{11}$$

$$p_\eta^2 = \frac{(s-m_\eta^2-q^2)^2 - 4m_\eta^2 q^2}{4s},\ \ \Gamma_\rho(q^2) = \Gamma_\rho(m_\rho^2)\frac{m_\rho^2}{q^2}(\frac{p_\pi^2(q^2)}{p_\pi^2(m_\rho^2)})^{\frac{3}{2}},\ \ p_\pi^2(q^2) = q^2/4 - m_\pi^2, \tag{12}$$

where $\sqrt{s} = E_{c.m.}$, $q$ is the $\pi^+\pi^-$ momentum, and

$$F(s) = \sum_V \frac{m_V^2 g_V e^{i\phi_V}}{s - m_V^2 + i\sqrt{s}\Gamma_V(s)} \tag{13}$$

with $V = \rho(770),\ \rho(1450),\ \rho(1700),\ \rho'''$. We introduce the complex parameter $g_V e^{i\phi_V}$, which is the combination $g_{V\rho\eta}/g_{V\gamma}$ of the coupling constants describing the transitions $V \to \rho\eta$ and $V \to \gamma^\star$, respectively.

The VMD formula (11) is used to fit to our cross-section data. The free fit parameters are $g_V$, masses and widths of the excited $\rho$-like states. The $\rho(770)$ mass and width are fixed at their PDG values [36]. Its phase $\phi_{\rho(770)}$ is set to zero. The coupling constants $g_{V\rho\eta}$ and $g_{V\gamma}$ are not expected to have sizable imaginary parts [8]. Therefore, we assume that $\phi_V$ for excited states may be 0 or $\pi$.

Models with one, two, or three excited states are tested. In Model 1 the cross section data are fitted in the energy range $E_{\mathrm{c.m.}} = 1.2 \div 1.70$ GeV with two resonances, $\rho(770)$ and $\rho(1450)$. The model with $\phi_{\rho(1450)} = 0$ fails to describe data. The fit result with $\phi_{\rho(1450)} = \pi$ is shown in Fig. 40 by the long-dashed curve. The obtained fit parameters are listed in Table 6. It is clearly seen that the fit with two resonances can not reproduce the structure of the cross section near 1.8 GeV.

In Models 2 and 3 we include an additional contribution from the $\rho(1700)$ resonance with phases $\phi_{\rho1700} = \pi$ and 0, respectively. The fits are done in the $E_{\mathrm{c.m.}} = 1.2 \div 1.90$ GeV range. The fit results are shown in Fig. 40 and listed in Table 6. Both models fit the data below 1.90 GeV reasonably well. Model 3 has better $\chi^2$ ($P(\chi^2) = 0.58$ instead of 0.03 for Model 2). Above 1.90 GeV the fitting curves lie below the data. The fit 4 includes arbitrary value of the phase $\phi_{\rho1700} = -1.1 \pm 0.4$ that is more close to zero instead of $\pi$.

Our fifth fit model includes a third excited state $\rho'''$. The fitted energy range is extended up to 2.2 GeV. The fitting curve is shown in Fig. 40. The fitted mass $m_{\rho'''} = 2.03 \pm 0.05$ GeV differs from the masses of

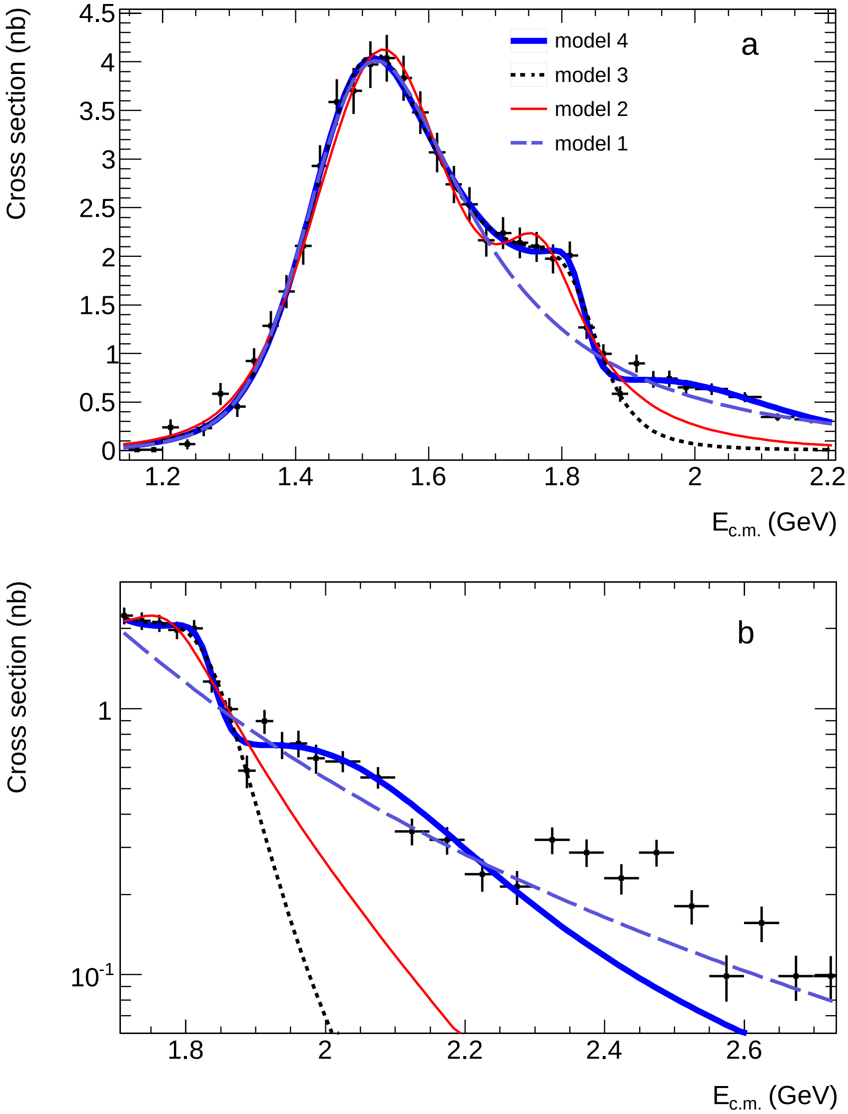

Figure 40: The measured $e^+e^- \to \pi^+\pi^-\eta$ cross section fitted with four models described in the text.

Table 6: The coupling constants, and resonance parameters obtained in the fits to the $e^+e^- \to \pi^+\pi^-\eta$ cross section data.

| Parameter | Model 1 | Model 2 | Model 3 | Model 4 | Model 5 |
|---|---|---|---|---|---|
| $g_{\rho(770)}$, GeV$^{-1}$ | $1.1 \pm 0.3$ | $2.3 \pm 0.3$ | $1.8 \pm 0.3$ | $1.4 \pm 0.3$ | $1.7 \pm 0.3$ |
| $g_{\rho(1450)}$, GeV$^{-1}$ | $0.49 \pm 0.02$ | $0.36 \pm 0.05$ | $0.44 \pm 0.02$ | $0.44 \pm 0.02$ | $0.46 \pm 0.03$ |
| $g_{\rho(1700)}$, GeV$^{-1}$ | – | $0.044 \pm 0.019$ | $0.080 \pm 0.012$ | $0.025 \pm 0.017$ | $0.015 \pm 0.008$ |
| $g_{\rho'''}$, GeV$^{-1}$ | – | – | – | – | $0.10 \pm 0.02$ |
| $m_{\rho(1450)}$, GeV/$c^2$ | $1.487 \pm 0.016$ | $1.54 \pm 0.01$ | $1.50 \pm 0.01$ | $1.49 \pm 0.01$ | $1.49 \pm 0.01$ |
| $m_{\rho(1700)}$, GeV/$c^2$ | – | $1.76 \pm 0.01$ | $1.83 \pm 0.01$ | $1.82 \pm 0.01$ | $1.83 \pm 0.01$ |
| $m_{\rho'''}$, GeV/$c^2$ | – | – | – | – | $2.03 \pm 0.05$ |
| $\Gamma_{\rho(1450)}$, GeV | $0.33 \pm 0.02$ | $0.31 \pm 0.03$ | $0.28 \pm 0.02$ | $0.31 \pm 0.02$ | $0.29 \pm 0.02$ |
| $\Gamma_{\rho(1700)}$, GeV | – | $0.16 \pm 0.04$ | $0.17 \pm 0.02$ | $0.12 \pm 0.04$ | $0.08 \pm 0.03$ |
| $\Gamma_{\rho'''}$, GeV | – | – | – | – | $0.47 \pm 0.18$ |
| $\phi_V$ | $0,\ \pi$ | $0,\ \pi,\ \pi$ | $0,\ \pi,\ 0$ | $0,\ \pi,\ (-1.1 \pm 0.4)$ | $0,\ \pi,\ 0,\ 0$ |
| $\chi^2/ndf$ | 14/16 | 35/21 | 19/21 | 18/20 | 26/26 |

the $\rho(1900)$ and $\rho(2150)$ states listed in the PDG table [36]. The model with three excited states successfully describe the $e^+e^- \to \pi^+\pi^-\eta$ cross section up to 2.3 GeV.

On the other hand, the noticeable change of the cross-section slope near 1.9 GeV may be interpreted as a threshold effect due to the opening of the nucleon-antinucleon production channel. Similar features near the nucleon-antinucleon threshold are seen in the processes $e^+e^- \to 3(\pi^+\pi^-)$ and $2(\pi^+\pi^-\pi^0)$ [31, 33, 34].

The fit is also performed with other parametrization. The parameters $g_V$ are replaced by the products

$$\Gamma(V \to e^+e^-)B(V \to \eta\pi^+\pi^-) = \frac{\alpha^2}{9\pi}\frac{|g_V|^2 m_V}{\Gamma_V}G(m_V^2). \tag{14}$$

From the fit in Model 3 we obtain:

$$\begin{aligned} &\Gamma(\rho(1450) \to e^+e^-)B(\rho(1450) \to \eta\pi^+\pi^-) = \\ &\qquad 210 \pm 24_{stat} \pm 10_{syst}\ \text{eV} \\ &\Gamma(\rho(1700) \to e^+e^-)B(\rho(1700) \to \eta\pi^+\pi^-) = \\ &\qquad 84 \pm 26_{syst} \pm 4_{syst}\ \text{eV} \end{aligned} \tag{15}$$

Model uncertainty of this parameters, primarily caused by strong overlapping of amplitudes, was estimated as 15% and 80% for $\rho(1450)$ and $\rho(1700)$, respectively. The obtained value $g_\rho = 1.8 \pm 0.3$ GeV$^{-1}$ for Model 3 is in reasonable agreement with the VMD estimation $1.57 \pm 0.07$ GeV$^{-1}$ based on data on the $\rho(770) \to \eta\gamma$ partial width [36].

The $e^+e^- \to \pi^+\pi^-\eta$ cross section in the energy range $E_{\text{c.m.}} = 3.0 \div 3.5$ GeV is measured for the first time. The data are shown in Fig. 37(b). The energy region near $J/\psi$ resonance (3.05–3.15 GeV) is excluded from the measurement. These data are fitted with a linear function. From the fit, we obtain the non-resonant cross section value at $E_{\text{c.m.}} = 3.1$ GeV to be $\sigma_{NR} = 0.047 \pm 0.008_{stat} \pm 0.005_{syst}$ nb.

## 8. CVC

The hypothesis of conservation of vector current (CVC), and isospin symmetry allows to express mass distribution of the $\pi^\pm\pi^0\eta$ system from the $\tau^\pm \to \pi^\pm\pi^0\eta\nu_\tau$ decay using the $e^+e^- \to \pi^+\pi^-\eta$ cross section, presumably dominated by isospin I=1 amplitude [30]. Using this relation, the $\tau$ decay branching fraction can

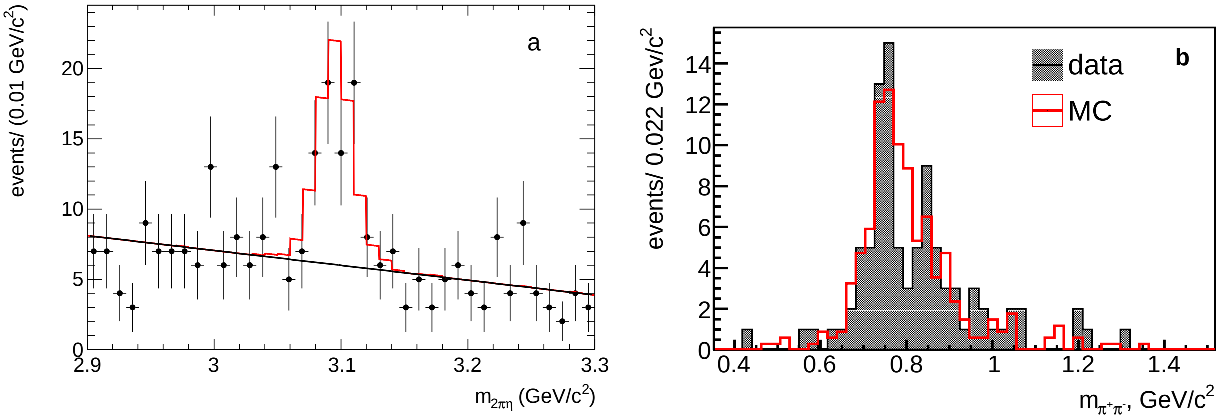

Figure 41: The $\pi^+\pi^-\eta$ (a) and $\pi^+\pi^-$ (b) invariant mass for the $J/\psi$ region.

be presented as integral:

$$\begin{gathered}\frac{\mathcal{B}(\tau^\pm\to\pi^\pm\pi^0\eta\nu_\tau)}{\mathcal{B}(\tau^\pm\to e^\pm\bar{\nu}_e\nu_\tau)} = \int_{(2m_\pi+m_\eta)^2}^{m_\tau^2} dq^2 \\ \sigma^{I=1}_{e^+e^-\to\pi^+\pi^-\eta}(q^2)\frac{3|V_{ud}|^2 S_{EW}}{\pi^+\pi^-\alpha^2}\frac{q^2}{m_\tau^2}(1-\frac{q^2}{m_\tau^2})^2(1+2\frac{q^2}{m_\tau^2}),\end{gathered} \tag{16}$$

where $q^2$ is the squared momentum of the $\pi^\pm\pi^0\eta$ system; $G_F$ - Fermi constant; $|V_{ud}|$ - corresponding element of CKM matrix; $S_{EW} = 1.0194$ is a factor taking into account electroweak radiative corrections. We use the following table values [36]: $m_\tau = 1.77682$ GeV/c$^2$; $\mathcal{B}(\tau^\pm\to e^\pm\bar{\nu}_e\nu_\tau) = 17.83\%$; $V_{ud} = 0.9742$.

We integrate Eq.16 using the fit function of $\sigma_{e^+e^-\to\pi^+\pi^-\eta}(q^2)$, reached in the previous section, and obtain the following result:

$$\begin{gathered}B^{\tau^-\to\pi^+\pi^-\eta}_{m_{\pi^+\pi^-\eta}<1.15} = 0.00083\%, \\ B^{\tau^-\to\pi^+\pi^-\eta}_{1.15<m_{\pi^+\pi^-\eta}<1.35} = 0.0147\pm0.0015\pm0.0015\%, \\ B^{\tau^-\to\pi^+\pi^-\eta}_{1.35<m_{\pi^+\pi^-\eta}<m_\tau} = 0.1460\pm0.00245\pm0.0065\%, \\ \mathcal{B}(\tau^\pm\to\pi^\pm\pi^0\eta\nu_\tau) = (0.1616\pm0.0026_{stat}\pm \\ 0.0080_{syst}\pm0.0011_{model})\% = (0.162\pm0.009)\%,\end{gathered} \tag{17}$$

where the first error represents the statistical uncertainty of measured cross section, the second error is corresponding to the systematic uncertainties listed in Table 3.

The model uncertainty is estimated using the difference between integration of Eq. 16 with the cross section fits performed under model 2 and 3, discussed in previous section. The calculation based on the previous *BABAR* measurement of the $\pi^+\pi^-\eta\to\pi^+\pi^-\pi^+\pi^-\pi^0$ final state [9] gives the result: $\mathcal{B}(\tau^\pm\to\pi^\pm\pi^0\eta\nu_\tau) = (0.1695\pm0.0085_{stat}\pm0.0136_{syst})\%$, and has a union part of the systematic errors with present result, such as uncertainties related with luminosity, radiative corrections, photon and track efficiencies, and triggers. This contribution is about 3%. The remaining systematic uncertainty due to signal calculation, background subtraction, and statistical errors is independent and can be averaged. Combining results of these two measurements we obtain: $\mathcal{B}(\tau^\pm\to\pi^\pm\pi^0\eta\nu_\tau) = (0.163\pm0.008)\%$.

The most precise direct measurement has been reported by Belle detector: $\mathcal{B}(\tau^-\to\pi^-\pi^0\eta\nu_\tau) = (0.135\pm0.003\pm0.007)\%$. Our CVC prediction deviates from this measurement by more than three standard deviations, that may indicate of a necessity to include isospin breaking corrections.

A final comparison is ploted in the Fig. 42.

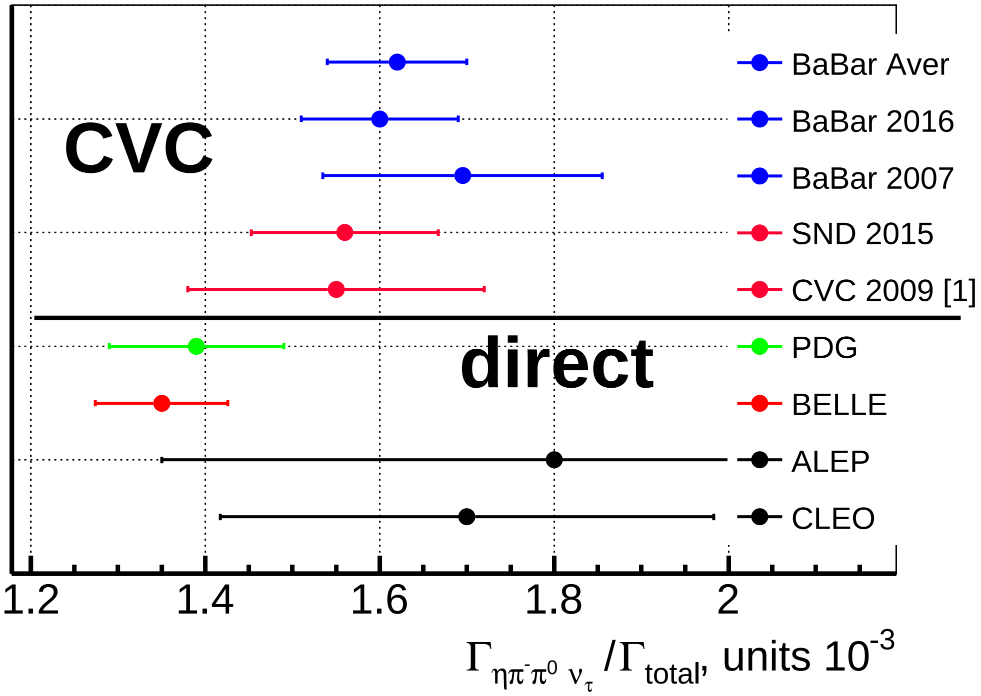

Figure 42: The comparison CVC predictions with direct measurements. The most precise direct measured has been done with Belle detector in 2009. "CVC 2009" corresponds to paper [32].

## 9. Influence on the prediction of $a_\mu$

Using the result for the $e^+e^- \to \pi^+\pi^-\eta$ cross section obtained in the present study, we compute the contribution of this channel to the anomalous magnetic moment of the muon $a_\mu$ via a dispersion relation in the energy region $E_{c.m.} < 1.8$ GeV:

$$a_\mu^{\pi^+\pi^-\eta}\cdot 10^{10} = \frac{1}{4\pi^3}\int_{thr}^{(1.8\ \text{GeV})^2} ds\cdot\sigma^{(0)}(s)\cdot K(s) = 1.185\pm 0.019\pm 0.058\pm 0.001, \tag{18}$$

where the first error is statistical, that is calculated by quadratic sum of the statistical uncertainties of obtained cross section; the seconf error is systematic; the third is model uncertainty. The last one was estimated as a difference of results of two $a_\mu$ calculations using the fit 3 result and the cross section values point by point.

## 10. $J/\psi$ region

The mass sprectrum of selected events in the region near $J/\psi$ mass are shown in the Fig. 41 (a). The distribution is approximated by the sum of $J/\psi$ signal and non-resonant background profiles. The signal profile is extracted from the simulation, when background is described by linear function. The fit yields $49 \pm 9$ events of the $J/\psi \to \pi^+\pi^-\eta$ decay. Figure 41 (b) shows the $m_{\pi^+\pi^-}$ invariant mass distribution for events from the $J/\psi$ peak, where strong interference of the $\rho\eta$ and $\omega\eta$ intermediate states is observed.

From obtained number of $J/\psi$ events we calculate a production $\Gamma_{J/\psi\to e^+e^-}\mathcal{B}_{J/\psi\to\pi^+\pi^-\eta}$ as:

$$\Gamma_{J/\psi\to e^+e^-}\mathcal{B}_{J/\psi\to\pi^+\pi^-\eta} = \frac{N_{J/\psi\to\pi^+\pi^-\eta}\cdot m^2_{J/\psi}}{6\pi^2\cdot dL/dE\cdot\varepsilon(m_{J/\psi})} = (2.34\pm 0.43_{stat}\pm 0.16_{syst})\ \text{eV}. \tag{19}$$

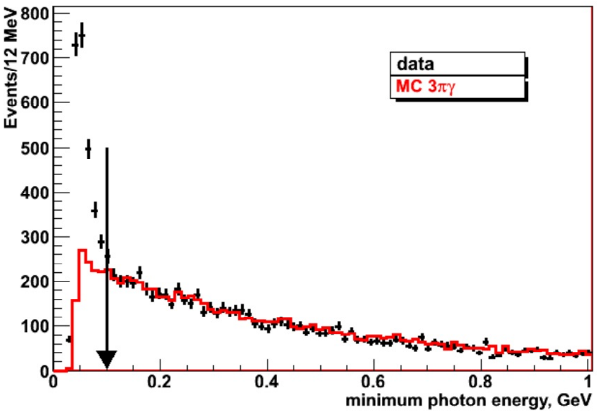

Figure 43: The minimal energy of photons from $\pi^0$ decay.

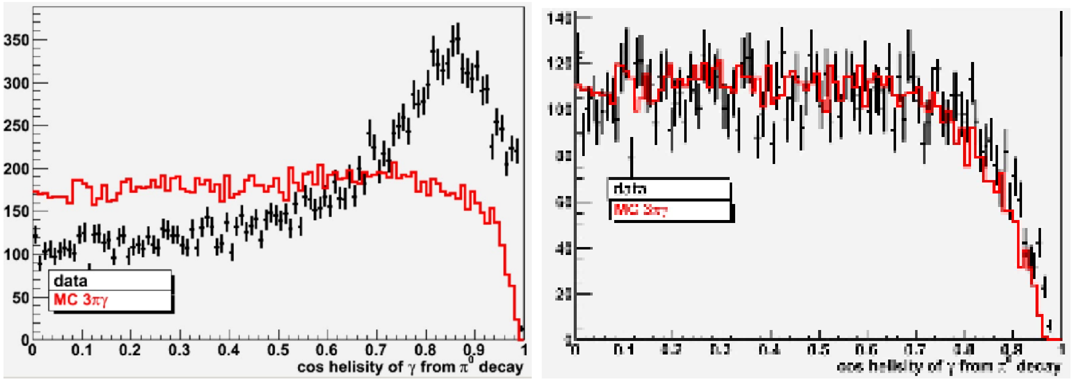

Figure 44: The helicity distributions before (top) and after (bottom) photon energy selection.

Using table value of the $J/\psi$ electron width ($5.55 \pm 0.14$ eV [36]), we calculate the branching fraction $\mathcal{B}(J/\psi \to \pi^+\pi^-\eta) = (0.042 \pm 0.008)\%$, which has better accuracy than the current table value $\mathcal{B}_{J/\psi\to\pi^+\pi^-\eta} = (0.040 \pm 0.017)\%$ [36].

Assuming the $J/\psi \to \rho\eta$ decay dominated by single photon exchange due to G-parity conservation, we can calculate the branching fraction using non-resonant cross section under the $J/\psi$ peak (see above) a using relation $\mathcal{B}_{J/\psi\to\rho\eta} = \frac{3}{4\pi\alpha^2} \cdot \mathcal{B}_{J/\psi\to e^+e^-} \cdot m^2_{J/\psi} \cdot \sigma_{NR} = (0.031 \pm 0.006)\%$. A reasonable agreement is observed with the table value for $\mathcal{B}_{J/\psi\to\rho\eta} = 0.019 \pm 0.002\%$ [36], which is significantly lower than $\mathcal{B}_{J/\psi\to\pi^+\pi^-\eta}$, that indicates about large contribution of $\omega\eta$ intermediate state with decay of $\omega$ meson into $\pi^+\pi^-$.

### *10.1.* $J/\psi \to 3\pi$

Event selection for $3\pi$ final state production is fully analogous to $2\pi\eta$ state. The range of the invariant mass of photons subjected to 5C kinematic fit is [0.10 : 0.16] GeV which corresponds to two photon production from $\pi^0$ decay. However, on three pion case its cross section significantly higher and background situation doesn't require using of multivariate analysis. Instead of TMVA response background can be suppressed by the requirement that minimal photon energy from $\pi^0$ decay is greater than 0.1 GeV. This distribution of minimal photon energy from $\pi^0$ decay is shown in the Fig. 43 with additional requests $\chi^2_{5C} < 40$ and $2.75 < m_{2\pi} < 3.5$ GeV . The background with low energy photons forming fake $\pi^0$ is rejected as shown by an arrow. The photon helicity (in other words —cos x—, where x - photons angle in $\pi^0$ rest frame) distributions before and after this cut are shown in the Fig. 44. It's clearly seen that background related with low photons in opposite to $\pi^0$ direction is effectively subtracted.

The Fig. 45 illustrates the $\chi^2_{5C}$ distribution. Points with error bars show the data events. The solid line shows the sum of the distributions for simulated $e^+e \to \pi^+\pi^-\pi^0\gamma$ and background processes. The shaded histogram shows the distribution for background processes among which the main is $q\bar{q}$ production. The selection $\chi^2_{5C} < 40$ is used for signal calculation.

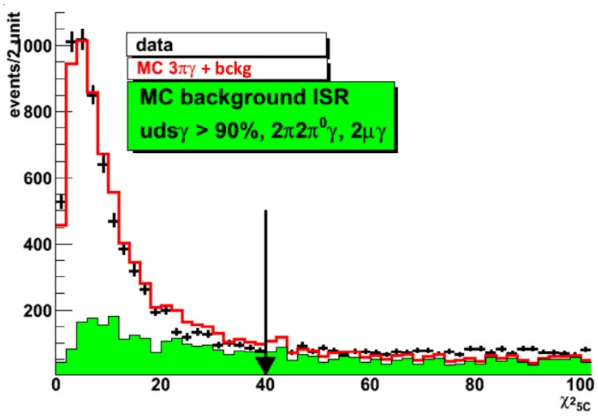

Figure 45: The $\chi^2$ distribution for events from the mass range $3.0 < m_{3\pi} < 3.2$ GeV/c$^2$.

The Fig. 46 illustrates $m_{3\pi}$ distribution near J/$\psi$ mass. The narrow J/$\psi$ width allows to use sideband method in order to define the number of signal events under J/$\psi$ peak: $N_{signal} = N(3 < m_{3\pi} < 3.2GeV/c^2) - N_{side}$. The calculation gives the result as $N_{signal} = 6141 \pm 97$. The dependence of the $N_{signal}$ on the low border of side band is presented in the bottom Fig. 46.

Monte-Carlo simulated efficiency equals $\epsilon_{MC} = 0.124 \pm 0.001$. The total efficiency of registration have be corrected as (6) due to differences in MC-data selections response. The correction related with $\chi^2_{5C}$ profiles can be calculated as $1 + \delta_\chi = \frac{N^{data}_{\chi^2<40}/N^{data}_{\chi^2<500}}{N^{MC}_{\chi^2<40}/N^{MC}_{\chi^2<500}}$. The fits of correspond $m_{3\pi}$ distributions are shown in the Fig. 47. Used profile is the sum of two gaussians for signal description and first order polinomial for background approximation. As a result the applied correction is $1 + \delta_\chi = 1.04 \pm 0.02$.

Also the event selection criteria contains requirement that two selected charged tracks wasn't identified as kaon using standard BaBar kaon id. The possible misidentification can be checked assuming independence of each pion to be fake defined as kaon. The correction is $1 + \delta_{Kid} = \frac{(1-\eta_{data})^2}{(1-\eta_{MC})^2}$, where $\eta$ - the probability of misidentification pion as kaon. If N1 - the number of $3\pi$ events with kaon absence requirement and N2 - number of $3\pi$ events with the requirement that number of identified kaons < 2 then $\frac{N2}{N1} = \frac{1-\eta^2}{1-\eta^2-2\eta(1-\eta)} = \frac{1-\eta^2}{(1-\eta)^2}$ and $\eta$ can be defined as $\eta = \frac{N2-N1}{N2+N1}$. The distributions related with N1 and N2 are shown in the Fig. 48. After N1 and N2 calculation using J/$\psi$ resonance approximation the probability of misidentification $\eta_{data} = 0.038 \pm 0.001$ and $\eta_{MC} = 0.0392 \pm 0.0004$ that correspond to $1 + \delta_{Kid} = 1.002 \pm 0.002$.

The production $\Gamma_{J/\psi \to ee} \cdot B_{J/\psi \to 3\pi}$ is calculated as (19): $\Gamma_{J/\psi \to ee} \cdot B_{J/\psi \to 3\pi} = 0.115 \pm 0.002_{stat} \pm 0.004_{syst}$ keV.

## 11. Summary

In this paper we have studied the process $e^+e^- \to \pi^+\pi^-\eta\gamma$, in which the photon is emitted from the initial state. Using the ISR technique we have measured the $e^+e^- \to \pi^+\pi^-\eta$ cross section in the c.m. energy range from 1.15 up to 3.5 GeV. Our results are in agreement with previous measurements and have comparable accuracy below 1.6 GeV and better accuracy above. In the energy range below 2.2 GeV the measured cross section is well described by the VMD model with four $\rho$-like resonances. Parameters of these resonances have been obtained.

Using measured cross section and the CVC hypothesis, the branching fraction of the decay $\tau \to \eta\pi^{\pm}\pi^{0}\nu_{\tau}$ has been predicted to be $B(\tau^{\pm} \to \pi^{\pm}\pi^{0}\eta\nu_{\tau}) = 0.162 \pm 0.009$ %.

From the measured number of $e^{+}e^{-} \to J/\psi\gamma \to \pi^{+}\pi^{-}\eta\gamma$ events we have determined the product $\Gamma_{J/\Psi\to e^{-}e^{+}}\mathcal{B}_{J/\psi\to\pi}$ $2.34 \pm 0.46$ eV, and branching fraction $\mathcal{B}(J/\psi \to \pi^{+}\pi^{-}\eta) = 0.042 \pm 0.008\%$.

From the measured number of events in the $e^{+}e^{-} \to J/\psi \to \pi^{+}\pi^{-}\eta\gamma, 3\pi\gamma$ reaction we determine the products $\Gamma_{J/\Psi\to e^{-}e^{+}}\mathcal{B}_{J/\psi\to\pi^{+}\pi^{-}\eta} = 2.34 \pm 0.46$ eV, corresponding to $\mathcal{B}(J/\psi \to \pi^{+}\pi^{-}\eta) = 0.042 \pm 0.008\%$. And $\Gamma_{J/\psi\to ee} \cdot B_{J/\psi\to 3\pi} = 0.115 \pm 0.002_{stat} \pm 0.004_{syst}$ keV.

[1] M., Benayoun *et al.*, Mod.Phys.Lett. A**14**, 2605-2614 (1999) hep-ph/9910523.

[2] A. Cordier, B. Delcourt, P. Eschstruth, F. Fulda, G. Grosdidier, J. Jeanjean, M. Jeanjean and R. J. Madaras et al., Nucl. Phys. B**172**, 13 (1980).

[3] A. Antonelli et al. [DM2 Collaboration], Phys. Lett. B**212**, 133 (1988).

[4] V. P. Druzhinin, M. S. Dubrovin, S. I. Eidelman, V. B. Golubev, V. N. Ivanchenko, A. P. Lysenko, E. V. Pakhtusova and A. N. Peryshkin et al., Phys. Lett.B**174**, 115 (1986).

[5] S. I. Dolinsky, V. P. Druzhinin, M. S. Dubrovin, V. B. Golubev, V. N. Ivanchenko, E. V. Pakhtusova, A. N. Peryshkin and S. I. Serednyakov et al., Phys. Rept.**202**, 99 (1991).

[6] R. R. Akhmetshin et al. [CMD-2 Collaboration], Phys.Lett. B**489**, 125 (2000) [hep-ex/0009013].

[7] M.N. Achasov et al. (SND Collaboration) JETP Lett. **92**, 80 (2010).

[8] V.M. Aulchenko et al., Phys. Rev. D **91**, 052013 (2015).

[9] Phys.Rev.D.**76**, 092005 (2007).

[10] N.N.Achasov, V.A.Karnakov, JETP Letters **39**, 285 (1984).

[11] M. K. Volkov*et al.*, Phys. Rev. C **89**, 015202 (2014).

[12] D. G. Dumm*et al.*, Phys. Rev. D **86**, 076009.

[13] BaBar Collaboration (Lees, J.P. et al.), Nucl. Instrum. Meth. A**726** (2013) 203-213; arXiv:1301.2703 [hep-ex].

[14] B.Aubert et al., Nucl. Instr. Meth. A **479**,1 (2002).

[15] V.P.Druzhinin, "Simulation of ISR processes with hard photon", http://www.slac.stanford.edu/BFROOT/www/Physics/ Tools/generators/AfkQed.ps.

[16] M.Caffo, H.Czyz, E.Remiddi, Nuo. Cim. **110A**, 515 (1997); Phys. Lett. **B327**, 369 (1994).

[17] E.BarBerio, B. van Eijk and Z. Was, Comput. Phys. Commun. **66**,115 (1991).

[18] S. Agostinelli et al. (Geant4 Collaboration), Nucl. Instrum. Methods Phys. Res., Sect. A **506**, 250 (2003).

[19] T. Sjostrand, Comput. Phys. Commun. **82**, 74 (1994).

[20] S. Jadach and Z. Was, Comput. Phys. Commun. **85**, 453 (1995).

[21] V. P. Druzhinin, Study of $e^{+}e$ annihilation at low energies, Presented at 23rd International Symposium on Lepton-Photon Interactions at High Energy (LP07), Daegu, Korea, 13-18 Aug 2007, published in Daegu 2007, Lepton and photon interactions at high energies 134, arXiv:0710.3455.

[22] A supporting document for a physics analysis BAD 2546.

[23] A supporting document for a physics analysis BAD 215.

[24] The report on PhiPsi conference 2015, China, http://indico.ihep.ac.cn/event/4464/session/0/contribution/22/ma

[25] B. P. Roe, H.-J. Yang, J. Zhu, I. Stancu, and G. McGre- gor, Nucl. Instrum. Methods Phys. Res., Sect. A **543**, 577 (2005).

[26] B. Aubert et al. (BaBar Collaboration), Phys. Rev. D **70**, 072004 (2004).

[27] B. Aubert et al. (BaBar Collaboration), Phys.Rev.D **80**, 052002 (2009

[28] J. P. Lees at al., Phys. Rev. D **85**, 112009 (2012).

[29] https://root.cern.ch/root/html304/TMatrixD.html

[30] Y.S.Tsai, Phys. Rev.D**4**,2821 (1971).

[31] J. Haidenbauer et al., Phys. Rev. D**92**, 054032(2015) [hep-ex/1506.08120].

[32] JETP Letters, Vol.**89**,No.9, pp.429431 (2009).

[33] A. E. Obrazovsky and S. I. Serednyakov, JETP Lett. **99**, 315 (2014).

[34] J. Haidenbauer, C. Hanhart, X. W. Kang and U. G. Meiner, Phys. Rev. D **92**, 054032 (2015).

[35] K.Inami*et al.*,Phys. Lett. B**672**, 209218 (2009).

[36] K. A. Olive et al. (Particle Data Group), Chin. Phys. C, **38**, 090001 (2014).

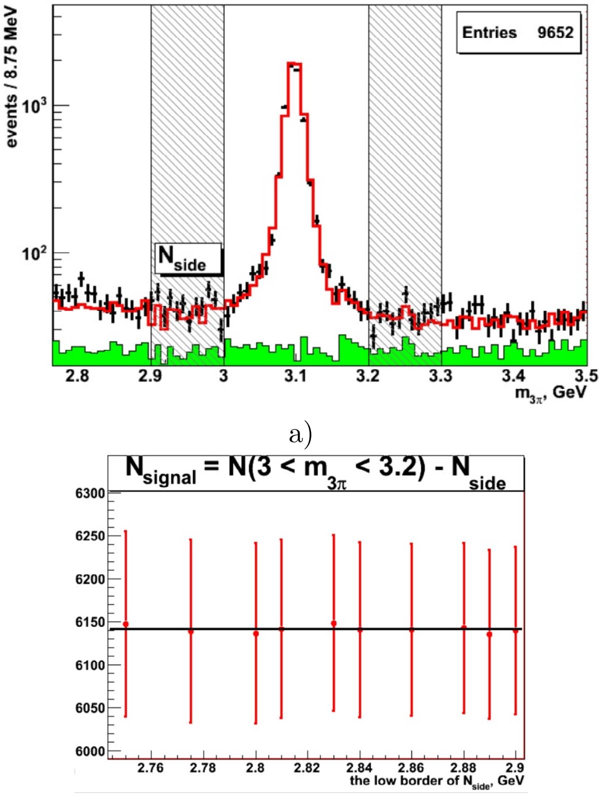

a)

b)

Figure 46: (a)The $m_{3\pi}$ distribution near J/$\psi$ resonance. Points with error bars show the data events. The solid line shows the sum of the distributions for simulated $e^+e \rightarrow \pi^+\pi\pi^0\gamma$ and background processes. The shaded histogram shows the distribution for background processes. (b) The number of obtained signal events $N_{signal}$ by the dependence on the low border of side band.

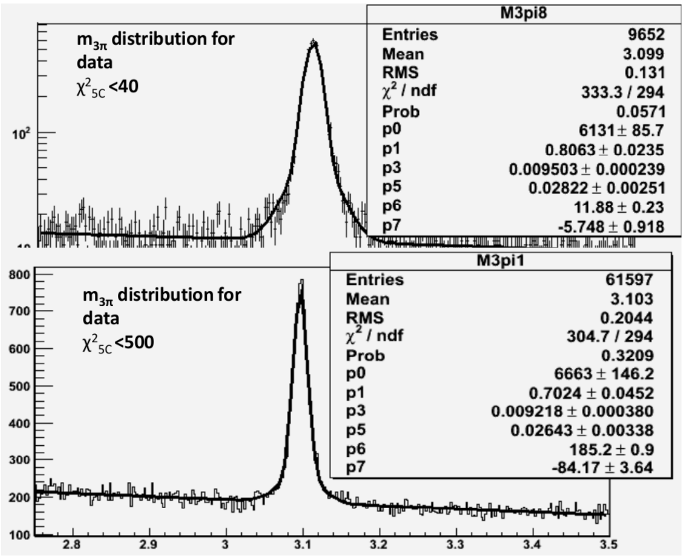

Figure 47: The approximation of $m_{3\pi}$ distributions near J/$\psi$ mass with different $\chi^2_{5C}$ criteria: $\chi^2_{5C} < 40$ - top and $< 500$ - bottom.

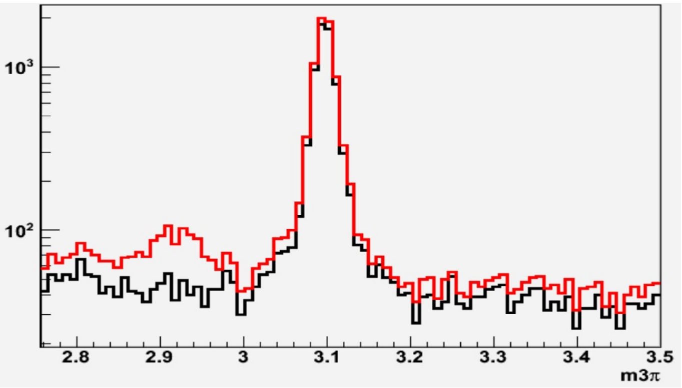

Figure 48: The $m_{3\pi}$ distribution near J/$\psi$ resonance with kaon absence requirement (black) and with requirement that only one as a maximum of selected tracks has KaonId == 1.